



RESEARCH ARTICLE

# Analysis and optimization design of motion characteristics for a 3-PUU/R parallel ankle joint rehabilitation mechanism

Xuechan Chen<sup>1,2</sup> , Jianxin Liu<sup>1,2</sup>, Jin an Dong<sup>1,2</sup> , Zhouhao Zhang<sup>1,2</sup>, Yu Guo<sup>1,2</sup>, Bo Xiao<sup>3</sup> and Ziming Chen<sup>1,2</sup>

<sup>1</sup>School of Mechanical Engineering, Yanshan University, Qinhuangdao, Hebei, China

<sup>2</sup>Parallel Robot and Mechatronic System Laboratory of Hebei Province, Yanshan University, Qinhuangdao, Hebei, China

<sup>3</sup>First Hospital of Qinhuangdao, Qinhuangdao, Hebei, China

**Corresponding author:** Ziming Chen; Email: [chenzm@ysu.edu.cn](mailto:chenzm@ysu.edu.cn)

**Received:** 8 May 2024; **Accepted:** 18 August 2024; **First published online:** 28 November 2024

**Keywords:** ankle joint ankle; parallel mechanism; kinematic analysis; motion/force transmission performance; mechanism

## Abstract

The large number of patients with ankle injuries and the high incidence make ankle rehabilitation an urgent health problem. However, there is a certain degree of difference between the motion of most ankle rehabilitation robots and the actual axis of the human ankle. To achieve more precise ankle joint rehabilitation training, this paper proposes a novel 3-PUU/R parallel ankle rehabilitation mechanism that integrates with the human ankle joint axis. Moreover, it provides comprehensive ankle joint motion necessary for effective rehabilitation. The mechanism has four degrees of freedom (DOFs), enabling plantarflexion/dorsiflexion, eversion/inversion, internal rotation/external rotation, and dorsal extension of the ankle joint. First, based on the DOFs of the human ankle joint and the variation pattern of the joint axes, a 3-PUU/R parallel ankle joint rehabilitation mechanism is designed. Based on the screw theory, the inverse kinematics inverse, complete Jacobian matrix, singular characteristics, and workspace analysis of the mechanism are conducted. Subsequently, the motion performance of the mechanism is analyzed based on the motion/force transmission indices and the constraint indices. Then, the performance of the mechanism is optimized according to human physiological characteristics, with the motion/force transmission ratio and workspace range as optimization objectives. Finally, a physical prototype of the proposed robot was developed, and experimental tests were performed to evaluate the above performance of the proposed robot. This study provides a good prospect for improving the comfort and safety of ankle joint rehabilitation from the perspective of human-machine axis matching.

## 1. Introduction

The ankle joint serves as a pivotal connection between the foot and the shank, enabling stabilization of the body and maintenance of balance during activities like walking, running, and jumping [1, 2]. Research has shown that ankle joint dysfunction is often caused by traumatic brain injury, stroke, and other neurological injuries, but it can also be caused by mechanical injuries such as ankle sprains [3]. After the ankle joint injury, it leads to excessive ligament relaxation and ankle joint instability, which is easy to cause repeated sprains. If the ankle joint injury is not timely rehabilitation treatment, it will affect the walking ability of patients and lead to muscle disuse atrophy, resulting in ankle joint dysfunction [4–6]. Its high incidence rate has led to ankle joint rehabilitation becoming a pressing medical and healthcare issue that requires resolution. In traditional ankle joint rehabilitation therapy, physical therapists typically conduct the rehabilitation training on the ankle joint. However, traditional treatment

methods are plagued by several issues: a severe shortage of rehabilitation medical beds, a lack of professional talent, and high rehabilitation costs. Moreover, there is a disparity in the professional technical level of physical therapists, making it difficult to achieve uniform quality in treatment. The development of ankle joint rehabilitation devices is urgently needed to address these issues and enhance patient care. With advanced technology, innovative devices can revolutionize ankle joint rehabilitation, leading to improved outcomes and better quality of life for patients.

Ankle rehabilitation mechanisms are usually designed based on the equivalent model of the ankle-foot complex, which is mainly divided into three categories. The first category equates foot movement to either a single DOF hinge joint model or a dual-rotation model. We discuss notable contributions from researchers, highlighting their proposed mechanisms. Lin [7] developed a single-DOF robot for ankle rehabilitation and evaluation, which can achieve three training modes, including passive traction, active tracking under constant external load, and control capability training. Saglia [8] proposed a high-performance 3-UPS/U ankle rehabilitation mechanism with two DOFs that can meet the rehabilitation needs of dorsiflexion/plantarflexion and inversion/eversion. Agrawal [9] designed an ankle movement correction biped rehabilitation robot with two DOFs, which can obtain the angular position of the rotating axis through encoders and sensors. Vallés [10] proposes a 3-RPS parallel ankle rehabilitation robot that has implemented passive, active assist, and active resistance exercises to train dorsiflexion/plantarflexion, varus, and valgus ankle movements. The second category equates foot movement to a spherical hinge model, divided into two modes: a fixed pivot point equivalence model and a drifting pivot point equivalence model. Li [11] equates the ankle joint to spherical hinge model and proposes a 3-DOF ankle rehabilitation mechanism, which adopts a series R mechanism and a 2UPS/RR parallel mechanism. Flores-Salazar [12] proposed 2PUS+RR mechanism for inversion/eversion and flexion/extension, adduction/abduction movements. Chang [13] addressed strong coupling and poor performance in ankle rehabilitation mechanisms by proposing a decoupled three-DOF ankle rehabilitation mechanism. Wang [14] introduced a redundant drive parallel ankle rehabilitation mechanism with 3-RUS/RRR configuration, which can achieve rotational movements of the ankle joint in three directions, offering better flexibility and stiffness suitable for rehabilitation exercises. Shi [15] proposed a 4UPS-RRR parallel ankle joint rehabilitation mechanism. The center of rotation of the rehabilitation institution can coincide with the height of the rotation center of the human ankle joint. Zeng [16] focused on real-time alignment issues and proposed a self-aligning parallel ankle rehabilitation robot (PSAAR) with “suitable passive DOF” to address joint rotation center alignment challenges. Dai [17] proposed a new reconfigurable ankle rehabilitation mechanism that can perform static and dynamic rehabilitation training, equating the ankle joint to a movable spherical joint model that can automatically match the joint compound of the ankle, and the dexterity of the mechanism varies smoothly throughout the entire working space. The third category equates foot movement to a dual-motion pair serial model. Wang [18] proposed a novel 2-UPS/RRR parallel ankle rehabilitation robot with a movable platform with adjustable rotation centers to accommodate the patient’s different ankle rotation centers. The third category equates foot movement to a double U-pair hinge model: Zhang [19, 20] proposed high-fit ankle joint models (UR, UU, and US) and presented a modular integrated design method, constructing a series of generalized spherical parallel mechanism ankle joint rehabilitation machines. Dul [21] equated the ankle-foot motion model to a spatial double-rotation serial mechanism, fully considering the influence of the talus on joint movement. Two kinematics pairs were used to fit the ankle and the subtalar joint, respectively, which is more reasonable than the spherical hinge model, but still has a difference compared to the actual ankle structure.

Previous studies have employed various models to represent the human ankle joint within rehabilitation devices, each with its own advantages. However, numerous studies have shown that the ankle-foot motion axis continuously changes throughout the entire range of motion [22–27]. Leardini [28] used visual motion capture technology to map the movement of the heel, talus, and fibula bones in the cadaveric specimen relative to the stationary tibia and found that most foot movements occur at the ankle joint, also sketching out the passive rotation axis of the ankle. Beimers [29] utilized CT scanning techniques to chart the movement of the foot between extreme positions and discovered that the inclination

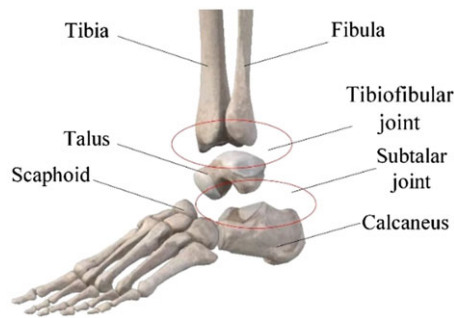


**Figure 1.** Bone structure of the ankle joint.

of the spiral axis during the extreme pronation and supination of the subtalar joint showed good consistency, whether combined with dorsiflexion/plantarflexion or not. Sheehan [30] collected sagittal data on the joints of the foot using cine-phase contrast magnetic resonance imaging technology and from this derived a complete kinematics description of each joint, drawing out the instantaneous spiral axes of the ankle, subtalar joint, and the root of the foot and tibia at different dorsiflexion/plantarflexion angles.

The designing an ankle rehabilitation robot based on the variations in the instantaneous axis of rotation of the human ankle joint can significantly enhance the comfort and safety of ankle rehabilitation. However, research capable of achieving a few DOFs parallel rehabilitation robot that fuses with the human ankle joint axis is quite limited. In view of this, this paper proposes a novel ankle rehabilitation mechanism from the perspective of the integration of the human-machine axis based on human movement characteristics. Within a certain range, this mechanism can continuously rotate around any axis within the spatial plane, meaning it can perform non-fixed-point rotation around instantaneous axis of the ankle, thus improving the rehabilitation effect, making it safer, and preventing secondary injury. Moreover, the mechanism offers a comprehensive range of ankle movements, including dorsiflexion, plantarflexion, inversion, eversion, internal rotation, external rotation, and stretching. These movements align with the basic movement patterns required for effective ankle rehabilitation.

This paper is divided into six sections. In Section 2, the variation pattern of the ankle axis is measured using a motion capture system to determine the range of motion. Section 3 presents the design of a 3-PUU/R parallel ankle rehabilitation mechanism, including inverse kinematics, complete Jacobian matrix, singular characteristics, and workspace analysis. Section 4 analyzes the motion/force transmission characteristics of the mechanism. In Section 5, the performance of the mechanism is optimized based on physiological characteristics to achieve optimal workspace and mechanical performance. Section 6 describes the manufacturing process of the ankle rehabilitation robot prototype.

## 2. Analysis of human ankle joint motion

### 2.1. The axis of motion of the human ankle and foot

The ankle joint structure of the human body is complex, as shown in Figure 1. Anatomically, the ankle joint can be divided into the tibiofibular joint and the subtalar joint. The tibiofibular joint encompasses the interaction between the tibia, fibula, and talus. The articular surfaces at the bottom of the tibia and fibula form the ankle mortise, which houses the talus. During dorsiflexion, the front end of the talus is fixed within the ankle mortise, restricting relative rotation. Conversely, during plantarflexion, a gap is created within the ankle mortise, allowing the talus to move freely. The subtalar joint, on the other hand, is composed of the talus, calcaneus, and navicular bones. Its posterior part is formed by the articulation of the protruding part of the talus with the concave part of the calcaneus, while its anterior part is embedded within the navicular bone. Due to the interaction of these anterior and posterior parts, the movement of the talus is somewhat restricted, endowing the subtalar joint with high stability.

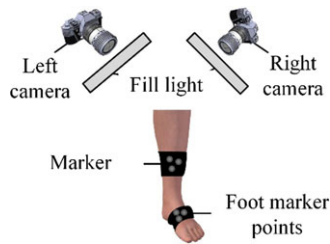


**Figure 2.** Positioning of landmark points.

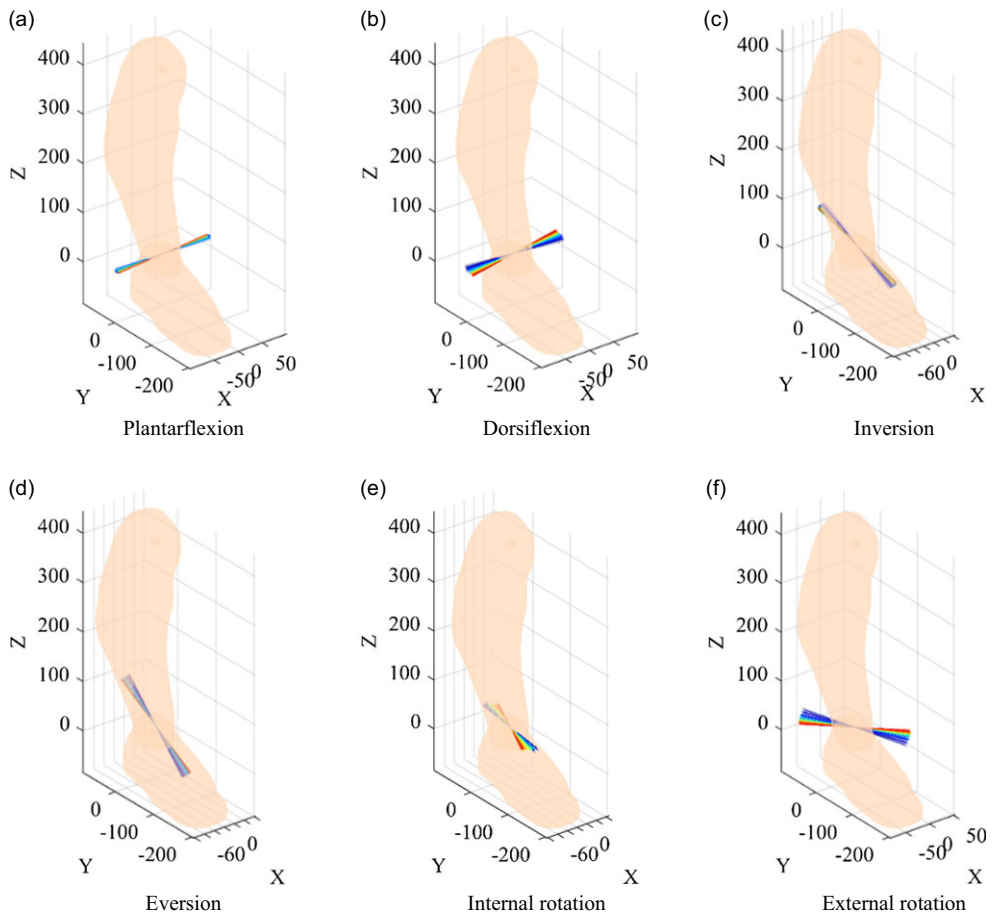


**Figure 3.** Axis of motion of the ankle joint.

During movement at the ankle joint, there is relative sliding between the bones. Therefore, we use a motion capture system to treat the lower leg and foot as two separate segments, placing markers on the dorsum of the foot and the area below the lower leg as shown in Figure 2. This allows us to measure the axis of motion of the human ankle joint during plantarflexion/dorsiflexion movements. As shown in Figure 3, it can be observed that the ankle joint does not move around a specific rotation center or axis, but rather that the axis of rotation is constantly changing.

Based on the above analysis, it can be observed that plantarflexion and dorsiflexion primarily involve movements around an axis nearly parallel to the X-axis, involving downward and upward movements of

Table I. Range of motion of the ankle joint.

Movement patterns	Plantarflexion	Dorsiflexion	Inversion	Eversion	Internal rotation	External rotation	Dorsal extension
Range of motion	0 ~ 30°	0 ~ 30°	0 ~ 20°	0 ~ 10°	0 ~ 25°	0 ~ 25°	0 ~ 20mm

the foot. Inversion and eversion are mainly lateral movements around an axis nearly parallel to the  $Y$ -axis, involving the foot turning inward and outward. Internal and external rotations are notable diagonal inward and outward rotational movements, involving the foot rotating internally and externally relative to the ankle joint. This multi-angle comparison helps us comprehensively understand the changes in the axis of motion of the ankle joint in different movement states. It is of great significance for accurately diagnosing movement patterns, evaluating the effects of exercise training, and formulating rehabilitation treatment strategies.

2.2. Range of motion of the human ankle and foot

The basic movements of the ankle joint are plantarflexion/dorsiflexion, eversion/inversion, internal rotation/external rotation, and dorsal extension. Due to differences in human anatomical structure, the range of motion at the ankle joint can vary slightly. According to statistical data [31] the range of motion for the ankle joint is presented in Table 1.

In order to ensure the safety and effectiveness of ankle joint rehabilitation, it is crucial for the axis of motion in the rehabilitation device to closely align with the human body axis. Taking into consideration the axis and range of motion of the human ankle joint, we have developed a novel rehabilitation robot that accurately replicates the precise axis of rotation of the ankle.

3. PUU/R mechanism description

This paper presents a novel axis-integrated 3-PUU/R serial-parallel ankle rehabilitation mechanism, as shown in Figure 4, ( $P$  represents a prismatic pair,  $U$  represents a universal pair, and  $R$  represents a rotational pair and the underlined letter denotes the driving joint) and the description of the mechanism is presented as follows: the 3-PUU/R ankle rehabilitation mechanism consists of three identical PUU limbs between a fixed platform  $A_1A_2A_3$  and a moving platform  $B_1B_2B_3$ . Additionally, a revolute pair is serially connected on the moving platform of the parallel mechanism, with the platforms denoted as  $F_1F_2F_3$ . The fixed and moving platforms are similar equilateral triangles, and each limb includes one  $P$  pair and two  $U$  pairs. To distinction the  $U$  pairs, the one connected to the moving platform is referred to as the fixed  $U$  pair, while the other one is referred to as the moving  $U$  pair. The axes of the  $i$ -th limb are defined by  $r_{i1}$ ,  $r_{i2}$ ,  $r_{i3}$ ,  $r_{i4}$ , and  $r_{i5}$ , respectively.  $O$ - $XYZ$  denotes the fixed coordinate system,  $P$ - $X_pY_pZ_p$  represents the moving coordinate system.  $A_i$  denotes the intersection point between the prismatic pair of the  $i$ -th limb and the fixed platform,  $U_i$  denotes the center of the moving  $U$  pair of the  $i$ -th limb, and  $B_i$  represents the center of the fixed  $U$  pair connected to the moving platform of the  $i$ -th limb.  $C$ - $X_oY_oZ_o$  is the coordinate system attached to the rotational platform on the moving platform, referred to as the pedal platform coordinate system.

The 3-PUU parallel mechanism satisfies the following geometric relationships: The direction of the prismatic pair is denoted by  $r_{i1}$ , the direction of the first rotational axis  $r_{i2}$  is aligned with the direction of the prismatic pair  $r_{i1}$ . The second rotational axis direction  $r_{i3}$  is perpendicular to the first rotational axis direction  $r_{i2}$ , and initially parallel to the fixed platform. The third rotational axis direction  $r_{i4}$  is parallel to the second rotational axis direction  $r_{i3}$ . The fourth rotational axis direction  $r_{i5}$  is perpendicular to the third rotational axis direction  $r_{i4}$ , the angle between the axis  $r_{i1}$  and the fixed platform is equal to the angle between the direction of the fourth rotational axis  $r_{i5}$  and the plane of the moving platform. The axis lines of the rotational pairs  $r_{i2}$  and  $r_{i5}$  in each limb intersect at points  $D_i$ . The axis lines of  $r_{i3}$

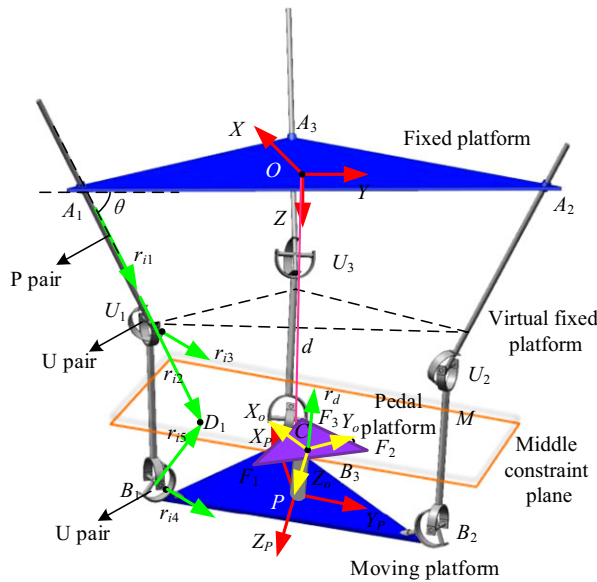


Figure 4. 3-PUU/R parallel mechanism.

and  $r_{i4}$  are both perpendicular to the axis line of the prismatic pair  $r_{i1}$ . The three points  $D_1$ ,  $D_2$ , and  $D_3$  determine a plane, which represents the middle constraint plane of the parallel mechanism. Under the fulfillment of the aforementioned geometric conditions and with the structural dimensions of the moving platform and fixed platform forming congruent triangles, the middle constraint plane is symmetric with respect to the moving platform and a virtual fixed platform. As shown in Figure 4, the middle constraint plane is symmetrical about both the moving platform and the virtual fixed platform, with the virtual fixed platform having the same size and shape as the moving platform, forming similar triangles with the fixed platform. The direction  $r_d$  of the rotational pair on the moving platform is perpendicular to the middle constraint plane and is located at the center position.

### 3.1. DOFs analysis of the 3-PUU/R mechanism

The parallel portion is analyzed by selecting one of the limbs and establishing a limb coordinate system as shown in Figure 5. The origin of the coordinate system of the  $i$ -th limb coincides with point  $D_i$ , the  $X_i$  axis is parallel to the  $r_{i3}$  axis, the  $Z_i$  axis is collinear with the  $r_{i2}$  axis, and the  $Y_i$  axis is determined by the right-hand rule.

In the limb coordinate system  $D_1-X_1Y_1Z_1$ , the kinematics screw representation of the PUU limb chain is expressed as follows:

$$\begin{cases} \$_{11} = (0 \ 0 \ 0; \ 0 \ 0 \ 1)^T \\ \$_{12} = (0 \ 0 \ 1; \ 0 \ 0 \ 0)^T \\ \$_{13} = (1 \ 0 \ 0; \ 0 \ a \ 0)^T \\ \$_{14} = (1 \ 0 \ 0; \ 0 \ b \ c)^T \\ \$_{15} = (0 \ c \ -b; \ 0 \ 0 \ 0)^T \end{cases} \quad (1)$$

where the parameters  $a$ ,  $b$ , and  $c$  are only related to the position of the joint of the mechanism. According to the screw theory, the reciprocal screw representation of the mechanism is derived as:

$$\$_1^r = (1 \ 0 \ 0; \ 0 \ 0 \ 0)^T \quad (2)$$

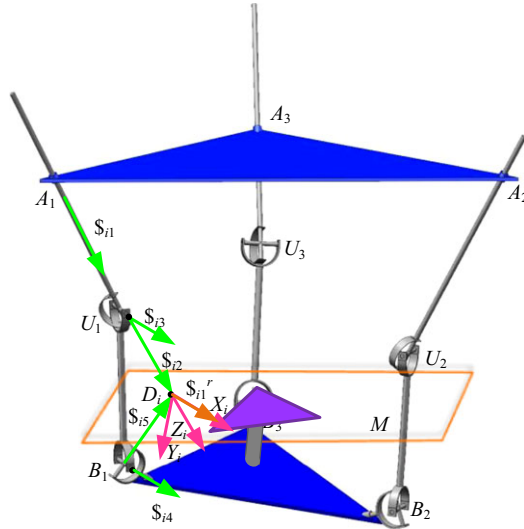


Figure 5. 3-PUU parallel mechanism.

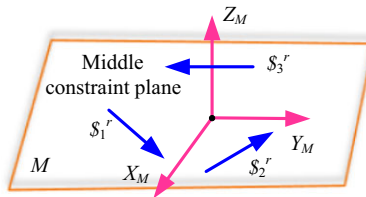


Figure 6. Middle constraint plane  $M$ .

Through the expression of the reciprocal screw, it can be seen that the reciprocal screw passes through the origin  $D_1$  of the limb coordinate system, and its direction coincides with the  $X_1$  axis. This line of constraint is perpendicular to  $r_{i1}$  and  $r_{i5}$ , and it lies on the middle symmetric plane  $M$ . Since the 3-PUU limbs of the planar mechanism are distributed symmetrically along a circle, all three lines of constraint are located on the middle symmetric plane  $M$ . To clearly express the relationship between the constraint screws, they are represented under a coordinate system  $O_M-X_M Y_M Z_M$ , where point  $O_M$  is an arbitrary point within the middle constraint plane  $M$ . The coordinate axes  $X_M$  and  $Y_M$  both lie within the constraint plane  $M$ , while the coordinate axis  $Z_M$  is perpendicular to the constraint plane  $M$ , as shown in Figure 6.

Within the coordinate system  $O_M-X_M Y_M Z_M$ , the three constraint screws are described by:

$$\begin{cases} \$1^r = (e_1 & e_2 & 0; & 0 & 0 & e_3)^T \\ \$2^r = (d_1 & d_2 & 0; & 0 & 0 & d_3)^T \\ \$3^r = (f_1 & f_2 & 0; & 0 & 0 & f_3)^T \end{cases} \quad (3)$$

According to equation (3), it can be observed that the moving platform is constrained in terms of its rotational DOF around the axis perpendicular to plane  $M$  and its two translational DOF parallel to the moving plane  $M$ . By taking the reciprocal screw of equation (3), we obtain the instantaneous kinematics screw of the moving platform as:

$$\begin{cases} \$1^m = (1 & 0 & 0; & 0 & 0 & 0)^T \\ \$2^m = (0 & 1 & 0; & 0 & 0 & 0)^T \\ \$3^m = (0 & 0 & 0; & 0 & 0 & 1)^T \end{cases} \quad (4)$$



According to equation (4), it can be observed that the 3-PUU parallel mechanism has three DOFs, which include rotational motion around any axis within plane  $M$  and translational kinematics along the normal direction of plane  $M$ .

The middle constraint plane corresponds to the plane formed by the origins of the three limb movement coordinate systems within the mechanism. The positions of the limb constraints pass through the limb coordinate system origins, and their directions align with the coordinate system axes. Throughout the kinematics of the mechanism, as long as no singular kinematics occurs, the positions of the limb constraints consistently lie on the middle constraint plane. Therefore, the constraint effect of the limb constraints on the moving platform of the mechanism remains unchanged, ensuring that the DOFs of the mechanism remain constant. In conclusion, a parallel mechanism with 2R1T and three DOFs can achieve continuous movement along any axis on the middle constraint plane.

A rehabilitation mechanism requires four DOFs to accommodate the range of changes in the ankle joint axis and meet the rehabilitation demands of the human ankle joint. Therefore, this study incorporates a revolute pair in series with the mobile platform of a parallel mechanism to obtain a hybrid serial-parallel mechanism with four DOFs, enabling movements such as plantarflexion, dorsiflexion, inversion, eversion, internal rotation, external rotation, and stretching.

### 3.2. Inverse kinematic solution for the hybrid serial-parallel PUU/R mechanism

#### 3.2.1. Posture description

The mechanism consists of both a parallel and a series part, with the parallel part having one translational and two rotational DOFs, while the series part has one rotational DOF. In the parallel part, the orientation of the moving platform of the 3-PUU mechanism is described by three parameters  $\alpha$ ,  $\beta$ ,  $d$ , as shown in Figure 7. The parameter for the series part is represented by  $\gamma$ . The origin  $O$  of the fixed coordinate system  $O$ - $XYZ$  is located at the center of the fixed platform, with the  $X$ -axis being perpendicular to  $A_1A_2$  and passing through the center of the fixed platform, the  $Z$ -axis being perpendicular to the fixed platform, and the  $Y$ -axis being determined by the right-hand rule. For the moving coordinate system  $P$ - $X_pY_pZ_p$ , the origin  $p$  is situated at the center of the movable platform, with the  $x_p$ -axis being perpendicular to  $B_1B_2$  and going through the center of the movable platform, the  $z_p$ -axis being perpendicular to the movable platform, and the  $y_p$ -axis being determined by the right-hand rule. On the moving platform, the coordinate system  $C$ - $X_oY_oZ_o$  has its origin  $C$  on the vertical line of the origin, with the  $X_o$ -axis parallel to the footrest  $F_1F_2$ , the  $Z_o$ -axis perpendicular to the footrest, and the  $Y_o$ -axis determined by the right-hand rule. Initially, the  $X$ ,  $X_p$ , and  $X_o$  axes are parallel.

The projection of the coordinate axis  $Z_p$  onto the  $XOY$  plane is defined as  $\mathbf{n}$ . The angle  $\alpha$  is the angle between the coordinate axis  $X$  and  $\mathbf{n}$ , while  $\beta$  is the angle between the coordinate axis  $Z_p$  and the  $Z$ -axis. The  $d$  represents the distance between point  $P$  and point  $O$ . The vector  $\mathbf{K}$  is defined as  $\mathbf{K} = \mathbf{n} \times \mathbf{Z}$ . Therefore, the moving platform coordinate system of the parallel mechanism is obtained by rotating the base platform coordinate system around the line  $\mathbf{K}$  by angle  $\beta$ . The pedal coordinate system placed on the moving platform is then rotated by angle  $\gamma$  around the  $Z_o$  axis.

In the parallel section, let  $\mathbf{K}$  be the unit vector  $\mathbf{K} = (k_x, k_y, 0)$ , and the transformation matrix is as follows:

$${}^O\mathbf{R}_p = \begin{bmatrix} k_x^2 \cdot \text{Ver}(c\beta) + c\beta & k_y k_x \cdot \text{Ver}(c\beta) & k_y s\beta \\ k_x k_y \cdot \text{Ver}(c\beta) & k_y^2 \cdot \text{Ver}(c\beta) + c\beta & -k_x s\beta \\ -k_y s\beta & k_x s\beta & c\beta \end{bmatrix} \quad (5)$$

where,  $s\beta = \sin \beta$ ,  $c\beta = \cos \beta$ ,  $k_x = \cos(\alpha + \frac{\pi}{2})$ ,  $k_y = \sin(\alpha + \frac{\pi}{2})$ ,  $\text{Ver}(c\beta) = (1 - \cos \beta)$

The transformation matrix from the pedal platform relative to the base platform is as follows:

$${}^O\mathbf{R}_r = {}^O\mathbf{R}_p \mathbf{R}(z_p, \gamma) \quad (6)$$



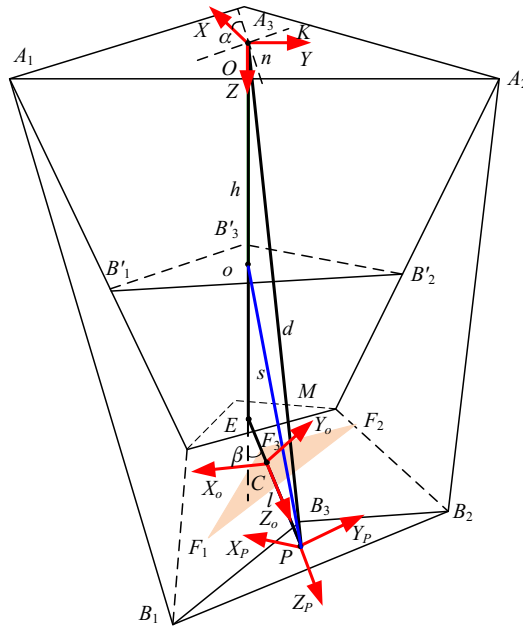


Figure 7. 3-PUU/R mechanism.

$${}^oR_r = {}^oR_p \begin{bmatrix} \cos \gamma & -\sin \gamma & 0 \\ \sin \gamma & \cos \gamma & 0 \\ 0 & 0 & 1 \end{bmatrix} \quad (7)$$

### 3.2.2. Inverse kinematics

Taking the prismatic pair of the 3-PUU mechanism on the moving platform and the revolute pair on the pedal as the actuation units, known with the positioning parameters  $\alpha$ ,  $\beta$ ,  $\gamma$ , and  $d$  of the pedal on the moving platform, solve for the length  $l_i$  of the prismatic pair and the rotation angle  $\eta$  of the revolute pair on the pedal. In the parallel section, since the fixed and moving platforms of the mechanism are not completely identical, as shown in Figure 7, the moving platform plane is represented by triangle  $B_1B_2B_3$ , and the virtual triangle  $B'_1B'_2B'_3$  symmetric about the middle constraint plane  $M$  is also shown. At the center of the moving platform, a revolute pair connected in series with the pedal is set, and the pedal plane is represented by triangle  $F_1F_2F_3$ . To more clearly explain the geometric relationship of the mechanism, the kinematics parameters between Figure 7 is presented in the form of Figure 8. The origin  $P$  of the moving platform is about the symmetric point of the middle constraint plane  $M$ , which is denoted as  $O$ . The pedal rotates  $\gamma$  around the  $Z_o$  axis. Set the following parameters  $|Oo| = h$ ,  $|oE| = h_r$ ,  $|CP| = l$ ,  $|oP| = s$ ,  $|OP| = d$ . The radius of the moving platform is  $r$ , the radius of the fixed platform is  $R$ , and range of the angle  $\theta$ :  $0 < \theta < 90$ .

Due to  $|MP| = |Mo|$

$$\angle OoP = \pi - \frac{\beta}{2} \quad (8)$$

According to Figure 8b, it can be obtained that:

$$h = (R - r) \tan \theta \quad (9)$$

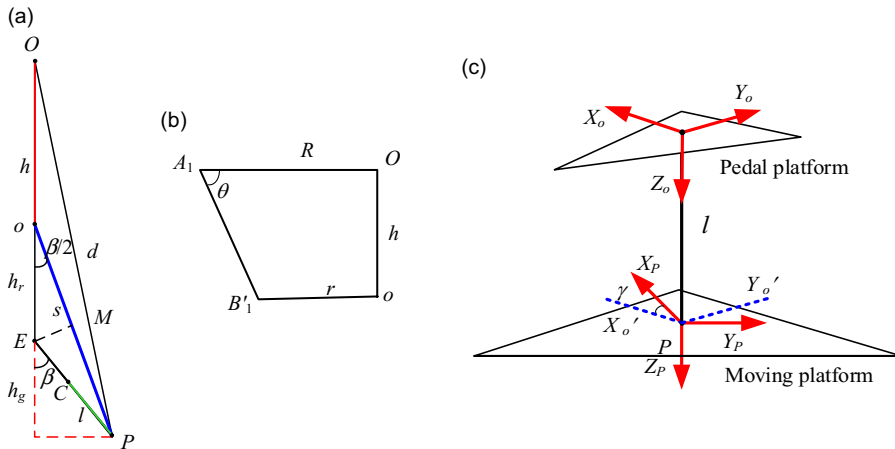


**Figure 8.** Inverse solution of the 3-PUU/R auxiliary mechanism.

In triangle  $OoP$ , applying the cosine theorem yields:

$$\cos\left(\pi - \frac{\beta}{2}\right) = \frac{s^2 + h^2 - d^2}{2sh} \quad (10)$$

$$P = \left[ s \sin \frac{\beta}{2} \cos \alpha \quad s \sin \frac{\beta}{2} \sin \alpha \quad h + s \cos \frac{\beta}{2} \right]^T \quad (11)$$

The coordinates of the center point  $A_i$  of the fixed platform  $P$  on the fixed coordinate system are given by:

$$\begin{cases} A_1 = R \cdot [\sin 30^\circ & -\cos 30^\circ & 0]^T \\ A_2 = R \cdot [\sin 30^\circ & \cos 30^\circ & 0]^T \\ A_3 = R \cdot [-1 & 0 & 0]^T \end{cases} \quad (12)$$

The coordinates of the center point  $B_i$  of the moving platform  $U$  on the moving coordinate system are given by:

$$\begin{cases} B_1 = r \cdot [\sin 30^\circ & -\cos 30^\circ & 0]^T \\ B_2 = r \cdot [\sin 30^\circ & \cos 30^\circ & 0]^T \\ B_3 = r \cdot [-1 & 0 & 0]^T \end{cases} \quad (13)$$

The coordinates of the center point  $B_i$  of the moving platform  $U$  in the fixed coordinate system are given by:

$$B_i = {}^O R_p \cdot B_i^p + P \quad (14)$$

Establishing the vector closed-loop equations for 3-PUU:

$$l_i L_i = A_i B_i - |U_i B_i| e_{UB,i} \quad (15)$$

$$A_i B_i = OP + PB_i - OA_i \quad (16)$$

Equation (15) is multiplied by itself on both sides of the dot, and the results obtained are collapsed to give:

$$l_i^2 + 2 |U_i B_i| L_i^T \cdot A_i B_i - A_i B_i^T \cdot A_i B_i + |U_i B_i|^2 = 0 \quad (17)$$

Solving Equation (17) gives the inverse solution of the solution:

$$l_i = \mathbf{L}_i^T \cdot \mathbf{A}_i \mathbf{B}_i \pm \sqrt{(\mathbf{L}_i^T \cdot \mathbf{A}_i \mathbf{B}_i)^2 - \mathbf{A}_i \mathbf{B}_i^T \cdot \mathbf{A}_i \mathbf{B}_i + |\mathbf{U}_i \mathbf{B}_i|^2} \quad (18)$$

where  $\mathbf{L}_i$  represents the unit direction vector of the prismatic pair,  $\mathbf{A}_i \mathbf{B}_i$  represents the direction vector from point  $\mathbf{A}_i$  to point  $\mathbf{B}_i$ ,  $l_i$  represents the distance of the prismatic pair,  $\mathbf{U}_i \mathbf{B}_i$  represents the direction vector from point  $\mathbf{U}_i$  to point  $\mathbf{B}_i$ , and  $\mathbf{e}_{UB,i}$  represents the unit direction vector of rod  $\mathbf{U}_i \mathbf{B}_i$ .

As can be seen from Equation (18), each branch drive has two solutions. Considering interference issues and the structure of the mechanism itself, only the negative square root in the formula can be considered as the inverse solution for this mechanism, thus the solution is unique.

The unit direction vector of  $\mathbf{e}_{CP} \cdot \mathbf{e}_{CP} = [\sin \beta \cos \alpha \sin \beta \sin \alpha \cos \beta]$ , then the coordinates of point  $\mathbf{C}$ , the origin of the pedal coordinate system, in the fixed coordinate system are:

$$\mathbf{C} = \mathbf{P} + l \cdot \mathbf{e}_{CP} \quad (19)$$

The angle of rotation  $\eta$  of the pedal platform is the angle between the  $X_O$  axis of the  $X_P Y_P$  plane in the moving platform coordinate system and the  $X_P$  axis, as shown in Figure 8c. Therefore,  $\eta = \gamma$ .

After determining the structure size parameters of the mechanism, the posture of the mechanism can be determined given the four parameters  $\alpha$ ,  $\beta$ ,  $\gamma$ , and  $d$  of the mechanism. The length parameters of each link and the rotation angle of the pedal platform can be obtained according to the above inverse solution.

Since the initial axis of rotation of the human ankle joint is oblique, adjustments to the position of the mechanism are required before rehabilitation can be performed on the human body. As shown in Figure 8a, the  $\triangle OEP$  is an isosceles triangle, therefore, the angle between line  $PE$  and the middle constraint plane  $M$  is:

$$\angle PEM = \frac{\pi}{2} - \frac{\beta}{2} \quad (20)$$

The line  $PE$  is perpendicular to the moving platform plane  $M$ , which means that the angle between the moving platform of the mechanism and the middle constraint plane  $M$  is  $\beta/2$ . For example, when it is necessary to meet the human body axis of  $7^\circ$  with the  $X$ -axis on the coronal plane and  $25^\circ$  with the  $X$ -axis on the horizontal plane, taking the mechanism parameters  $\alpha = 25^\circ$  and  $\beta = 16^\circ$  can satisfy the adjustment of the initial posture of the mechanism.

$$h_r = \frac{h_g}{\cos \beta} \quad (21)$$

where  $h_g$  represents the height of the ankle joint for different individuals, and  $h_r$  denotes the distance from point  $p$  the origin of the moving system to point  $E$ .

According to the Pythagorean theorem:

$$d = \sqrt{(h_g + h_r + h)^2 + (h_g \times \tan \beta)^2} \quad (22)$$

By using Equation (22), we can obtain the appropriate angle pose adjustment for different ankle heights. It fulfills the requirement for initial rehabilitation pose adjustment under the left/right foot rehabilitation mode needed by patients with diverse conditions.

### 3.2.3. The complete Jacobian matrix

The Jacobian matrix of a parallel mechanism is a critical method for analyzing its kinematics performance and singularity. It represents the mapping relationship between the joint input speeds and the output speeds of the moving platform. Utilizing screw theory, the full Jacobian matrix of this parallel mechanism has been established.

The output kinematics screw of the moving platform can be written as  $\$_p = [\omega^T \ v^T]^T$ , where  $\omega$  denotes the instantaneous angular velocity of the moving platform, and  $v$  represents the instantaneous velocity vector that is affixed to the moving platform and coincides with the origin  $O$  of the base platform.

The output kinematics screw of the moving platform can be represented as a linear superposition combination of the kinematics screws of each PUU limb, considering that each PUU limb has 5 DOFs:

$$\mathbf{\$}_p = \dot{d}_i \hat{\mathbf{\$}}_{i1} + \dot{\theta}_{i2} \hat{\mathbf{\$}}_{i2} + \dot{\theta}_{i3} \hat{\mathbf{\$}}_{i3} + \dot{\theta}_{i4} \hat{\mathbf{\$}}_{i4} + \dot{\theta}_{i5} \hat{\mathbf{\$}}_{i5}, i = 1, 2, 3 \quad (23)$$

where  $\dot{d}_i$  represents the linear velocity of the prismatic pair in the  $i$ -th limb,  $\dot{\theta}_{ij}$  denotes the angular velocity of the  $j$ -th kinematics pair unit kinematics screw in the  $i$ -th limb, and  $\hat{\mathbf{\$}}_{ij}$  refers to the unit screw of the  $j$ -th joint in the  $i$ -th limb.

By taking the reciprocal screw of the limb screw system, it is found that the 3-PUU parallel mechanism has three constraint inverse screws, which pass through points  $D_i$  on the constraint plane and are parallel to the axes  $r_{i3}$  of the revolute pair. Since the limb constraints and the limb screw kinematics pairs are mutually inverse, it follows that:

$$\hat{\mathbf{\$}}_{r11}^T \mathbf{\$}_p = 0 \quad (24)$$

$$\text{where } \hat{\mathbf{\$}}_{r11} = \begin{bmatrix} s_{13} \\ E_1 \times s_{13} \end{bmatrix}, \hat{\mathbf{\$}}_{r21} = \begin{bmatrix} s_{23} \\ E_2 \times s_{23} \end{bmatrix}, \hat{\mathbf{\$}}_{r31} = \begin{bmatrix} s_{33} \\ E_3 \times s_{33} \end{bmatrix}.$$

By writing the three limbs in matrix form, we obtain

$$\mathbf{J}_c \mathbf{\$}_p = 0 \quad (25)$$

$$\text{where } \mathbf{J}_c = \begin{bmatrix} (E_1 \times s_{13})^T & s_{13}^T \\ (E_2 \times s_{23})^T & s_{23}^T \\ (E_3 \times s_{33})^T & s_{33}^T \end{bmatrix} \text{ denotes the Jacobian matrix of the } \mathbf{J}_c \text{ constraint.}$$

If the actuation joint of the  $i$  limb is locked, the rank of the constraint screw system increases, yielding a new constraint wrench screw  $\hat{\mathbf{\$}}_{r12}$ , which is oriented along axis  $U_i B_i$  with an intercept of 0.

The actuation force of the  $i$ -th limb can be represented as:

$$\hat{\mathbf{\$}}_{r12}^T = [s_{i6} \quad B_i \times s_{i6}] \quad (26)$$

where  $s_{i6}$  represents the unit vector along the direction of each link  $U_i B_i$ .

Multiplying both sides of Equation (23) by  $\hat{\mathbf{\$}}_{r12}^T$ , we have:

$$\hat{\mathbf{\$}}_{r12}^T \mathbf{\$}_p = \hat{\mathbf{\$}}_{r12}^T (\dot{d}_i \hat{\mathbf{\$}}_{i1} + \dot{\theta}_{i2} \hat{\mathbf{\$}}_{i2} + \dot{\theta}_{i3} \hat{\mathbf{\$}}_{i3} + \dot{\theta}_{i4} \hat{\mathbf{\$}}_{i4} + \dot{\theta}_{i5} \hat{\mathbf{\$}}_{i5}), i = 1, 2, 3 \quad (27)$$

Since the limb actuation screw  $\hat{\mathbf{\$}}_{r12}$  of the limb is reciprocal with all the other moving screws except for the moving screw, it follows that:

$$\hat{\mathbf{\$}}_{r12}^T \mathbf{\$}_p = \dot{d}_i \hat{\mathbf{\$}}_{r12}^T \hat{\mathbf{\$}}_{i1}, i = 1, 2, 3 \quad (28)$$

The kinematics of the prismatic pair in the limb is represented by  $\hat{\mathbf{\$}}_{i1} = (0 \quad s_{i1})$ , and therefore, it can be determined that:

$$\begin{bmatrix} s_{16} & s_{26} & s_{36} \\ B_1 \times s_{16} & B_2 \times s_{26} & B_3 \times s_{36} \end{bmatrix}^T \mathbf{\$}_p = \begin{bmatrix} s_{16} & s_{26} & s_{36} \\ B_1 \times s_{16} & B_2 \times s_{26} & B_3 \times s_{36} \end{bmatrix}^T \begin{bmatrix} 0 & s_{11} \\ 0 & s_{21} \\ 0 & s_{31} \end{bmatrix}^T \dot{d}_i \quad (29)$$

The Equation (30) is arranged in matrix form:

$$\mathbf{J}_x \begin{bmatrix} v \\ \omega \end{bmatrix} = \mathbf{J}_t \dot{d}_i \quad (30)$$

Then:

$$\mathbf{J}_a \begin{bmatrix} v \\ \omega \end{bmatrix} = \dot{d}_i \quad (31)$$

where  $\mathbf{J}_a = \begin{bmatrix} \frac{s_{16}^T}{s_{11} \cdot s_{16}} & \frac{(B_1 \times s_{16})^T}{s_{11} \cdot s_{16}} \\ \frac{s_{26}^T}{s_{21} \cdot s_{26}} & \frac{(B_2 \times s_{26})^T}{s_{21} \cdot s_{26}} \\ \frac{s_{36}^T}{s_{31} \cdot s_{36}} & \frac{(B_3 \times s_{36})^T}{s_{31} \cdot s_{36}} \end{bmatrix}$  represents the mechanism actuation Jacobian matrix.

By combining Equations (25) and (31), we obtain the completed Jacobian matrix of the mechanism as:

$$\dot{\mathbf{q}} = \mathbf{J} \dot{\mathbf{s}}_p \quad (32)$$

where  $\mathbf{J} = \begin{bmatrix} \mathbf{J}_a \\ \mathbf{J}_c \end{bmatrix}_{6 \times 6}$ ,  $\dot{\mathbf{q}} = [\dot{d}_1 \quad \dot{d}_2 \quad \dot{d}_3 \quad 0 \quad 0 \quad 0]^T$ ,  $\dot{q}_1, \dot{q}_2, \dot{q}_3$  represent the input speeds of the three prismatic pairs, respectively.

### 3.2.4. Singularity analysis

The singular configuration of the series-parallel hybrid mechanism is only related to the 3-PUU parallel part, and the R pair in series does not affect it, so only the 3-PUU parallel part is analyzed. Based on the relationship between the input velocity and the output velocity of the mechanism complete Jacobian matrix, the singularity of the mechanism is analyzed. Utilizing equations (30), the 3-PUU mechanism under study is considered singular when either matrix  $\mathbf{J}_x$  or  $\mathbf{J}_l$ , or both, are rank-deficient. We will discuss the following three different cases:

1. The condition for the first singularity is:

$$\text{rank}(\mathbf{J}_l) < 3 \text{ and } \text{rank}(\mathbf{J}_x) = 3 \quad (33)$$

When this singularity occurs, the moving platform loses one or more degrees of freedom, and the mechanism must meet the following conditions:

$$\mathbf{E}_i^T \mathbf{L}_i = 0 \quad (34)$$

where  $\mathbf{E}_i$  represents the unit direction vector of the  $U_i B_i$  links, and  $\mathbf{L}_i$  represents the unit direction vector of the prismatic pairs.

In this case, vector  $\mathbf{E}_i$  and vector  $\mathbf{L}_i$  are perpendicular to each other. There are two configurations of the 3-PUU mechanism. The first position is shown in Figure 9a, in which the moving platform and branch will interfere. This situation should be avoided in the actual situation, although by changing the size parameters of the mechanism, as shown in Figure 9a, the singularity will also occur, but the overall size of the mechanism is relatively extreme at this time. In practice, the situation when the first singularity occurs is shown in Figure 9b.

The first singularity also occurs when the mechanism meets the following conditions:

$$\mathbf{L}_i = 0 \quad (35)$$

In this case, the length of the prismatic pair is 0. When the problem of interference is considered in a practical situation, the conditions required by formulas  $\mathbf{L}_i = 0$  do not occur.

2. The second singularity occurs under the following conditions:

$$\text{rank}(\mathbf{J}_l) = 3 \text{ and } \text{rank}(\mathbf{J}_x) < 3 \quad (36)$$

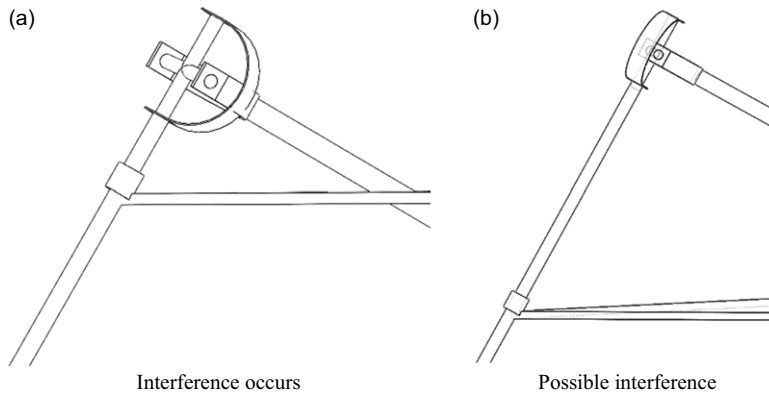


**Figure 9.** First kind of singular position.

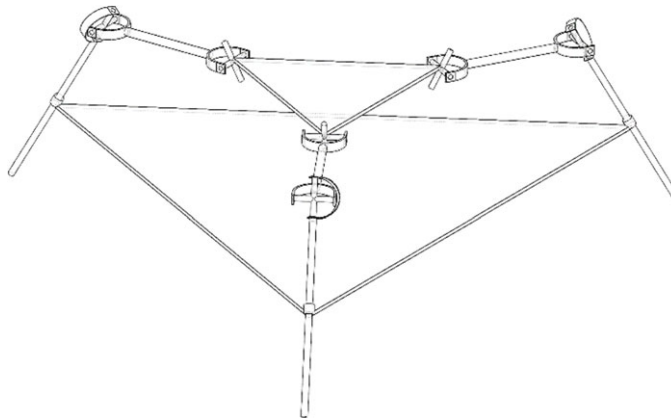


**Figure 10.** Second kind of singular position.

When this singularity occurs, the moving platform can still move even if all the drives are locked and the moving platform cannot resist one or more forces or torques even if all the drives are locked. This singularity occurs when the matrix  $\mathbf{J}_x$  satisfies:

$$\mathbf{b}_i \times \mathbf{E}_i^T = 0 \quad (37)$$

where  $\mathbf{b}_i$  represents the vector from the center of the moving platform to the center point of  $\mathbf{B}_i$ .

According to the complete Jacobian matrix obtained above, each row in the driving Jacobian matrix  $\mathbf{J}_x$  represents a wrench screw coaxial with the corresponding limb prismatic pair. When the rank of  $\mathbf{J}_x$  decreases, the mechanism will have driving singularity. For the 3-PUU parallel mechanism, this means that the three driving wrench screws become linearly related, which occurs when these three screws are either coplanar and intersecting, coplanar and parallel, or coaxial – these positions constitute the driving singularity configurations. Given that the three limbs are arranged obliquely with a  $120^\circ$  rotational symmetry, only the configuration where the driving force wrenches are coplanar and intersecting is theoretically possible. However, in this case, the moving and fixed platforms of the 3-PUU mechanism are in a parallel state, as shown in Figure 10. The moving and fixed platforms are equilateral triangles. During driving singularity, the length of the prismatic pair would be 0. Considering the practical situation, the driving singularity will not occur.

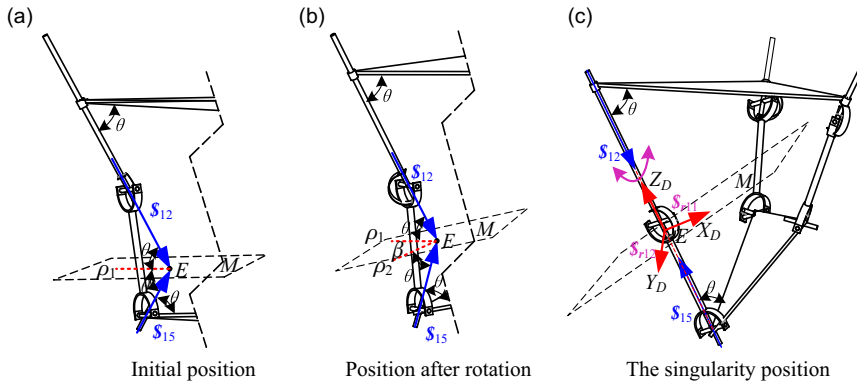


Figure 11. Limb singularity.

At this time, the three middle connecting links of the moving platform are parallel to the plane where the moving platform is located. At this time, when all the drives are locked, the moving platform of the mechanism can have a small movement.

### 3. The third singularity occurs under the following conditions:

This singularity is a little different from the previous two in that it requires the mechanism to satisfy some special conditions on the dimensional parameters. When this singularity occurs, the mechanism must meet the following conditions:

$$E_i^T = 0 \quad (38)$$

For the 3-PUU parallel mechanism proposed in this paper, when the third singularity occurs, when the third singularity occurs, the two link lengths between two universal joints in the same limb become 0. That is, two universal hinges on the same limb coincide. It is clear that this singularity is not possible in practice.

By this method, in addition to the above three kinds of singularities, the 3-PUU parallel mechanism studied in this paper has other singularities, which cannot be obtained by analyzing whether the matrices  $J_l$  and  $J_x$  in the formula are full rank, such as constraint singularity.

Referring to the method of Fang [32], the singularity problem of parallel mechanism is analyzed, which can be divided into three types: limb singularity, platform singularity, and driving singularity. The driving singularity is in the same position as the singularity in Figure 10 above, and only the remaining two are analyzed below.

Limb singularity refers to the linear correlation of the kinematics screw within a limb, which leads to the rank reduction of the limb kinematics screw. Taking the first limb as an example for analysis, when the mechanism kinematics, as shown in Figure 11. When the limb kinematics screw  $s_{11}$ ,  $s_{12}$ , and  $s_{15}$  are collinear, the mechanism limb singularity occurs. In such a case, the limb coordinate system is established, as shown in Figure 11c, with the origin located at point  $E$ , where the axis of  $r_{12}$  is parallel to that of  $r_{15}$  and intersects with the constraint plane. The  $z_m$  axis is oriented in the same direction as the prismatic pair axis, the  $x_m$  axis is aligned with the revolute pair axis  $r_{13}$ , and the  $y_m$  axis is determined by the right-hand rule. According to the screw theory, at this moment, the limb provides two constraints, which is an addition of a couple of constraints  $s_{r12}$  along the  $y_m$  axis, which restrains the rotation around the  $y_m$  axis, thus reducing the DOFs of the mechanism.

To reveal the relationship between the limb singularity of the parallel mechanism and its parameters, the kinematic screws of joints  $R_{12}$ ,  $R_{13}$ , and  $R_{15}$  are expressed in Plücker coordinates:  $(s_{12}; s_{120})$ ,



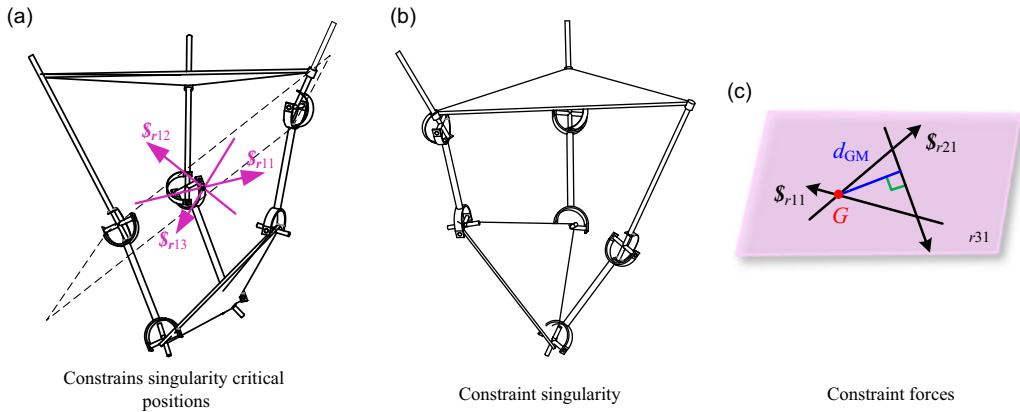


**Figure 12.** Mechanism platform singularity.

$(s_{i3}; s_{i30}), (s_{i5}; s_{i50})$ . The angle of rotation between  $-s_{i2}$  and  $-s_{i5}$  around  $s_{i3}$  is denoted as  $\delta_i$ , which can be solved using MATLAB atan2 function, as follows:

$$\delta_i = \text{atan2}((( -s_{i2}) \times (-s_{i5})) \cdot s_{i3}, (-s_{i2}) \cdot (-s_{i5})) \cdot 180/\pi \quad (39)$$

When any of the angles  $\varphi_1, \varphi_2, \varphi_3$  reaches  $180^\circ$ , the limb singularity occurs. When the moving platform is parallel to the fixed platform, the following geometric conditions are easily obtained:

$$\delta_i = 2\theta \quad (40)$$

During the rehabilitation exercises for ankle joints, it is crucial to ensure that the mechanism remains free from any limb kinematics singularities across the entire range of rehabilitation movements. The angles of the mechanism need to meet certain requirements.

Firstly, the relationship between the rotation angle  $\beta$  of the moving platform and the angle  $\delta_1$  between the central axes of the revolute pairs  $r_{i2}$  and  $r_{i5}$  when the limb singularity occurs is analyzed. After a certain rotation of the mechanism moving platform, draw a straight line  $\rho_1$  parallel to the fixed platform at the intersection point  $E$  of the constraint plane and the central axis, and a straight line  $\rho_2$  parallel to the moving platform. At this moment, it can be observed that  $\delta_1 = 2\theta + \beta$ . When the mechanism fixed platform and moving platform are parallel, we obtain  $\beta = 0^\circ, \delta_1 = 2\theta$  is also obtained. During a limb kinematics singularity of the mechanism, the angle between the central axes of revolute pairs  $r_{i2}$  and  $r_{i5}$  is  $180^\circ$ , which corresponds to  $\delta_1 = 2\theta + \beta = 180^\circ$ . Therefore, to avoid limb kinematics singularities in the mechanism, it is essential to ensure that the angle  $\delta_1$  between the central axes of revolute pairs  $r_{i2}$  and  $r_{i5}$  in the ankle joint rehabilitation mechanism is less than  $180^\circ$ , hence  $\theta$  should be less than  $180^\circ$ . Therefore, it is essential to ensure that the mechanism does not encounter limb kinematics singularities during the rehabilitation exercise by carefully selecting the mechanism parameters  $\theta$ .

The platform constraint singularity refers to the linear correlation of the constraint screw system of the moving platform, thereby increasing the DOFs of the mechanism. In this paper, each limb of the 3-PUU mechanism exerts a constraint on the moving platform, with these three constraints located within the same plane. Under the action of these three constraints, the mechanism has a 2RIT kinematics. However, if the three limb constraints are relatively positioned at one point or are parallel, the three constraints become linearly correlated, resulting in a reduction of the number of constraints on the moving platform. This situation is known as a platform singularity. In this case, the constraints of the mechanism intersect at a single point, as shown in Figure 12a, and the mechanism gains an additional rotational DOF perpendicular to the constraint plane  $M$ , transforming into a 3RIT parallel mechanism, as shown in Figure 12b.

Due to the  $120^\circ$  rotational symmetry of the mechanism, it suffices to analyze a single range. The constraint forces are shown in Figure 12c, where the intersection point of the constraint forces

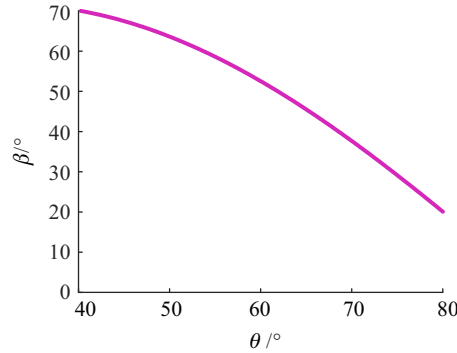


**Figure 13.** Relationship between mechanism platform singularity and angular displacement.

from the first and second limbs is  $G$ . The coordinates of  $G$  in the global coordinate system can be expressed as:

$$\mathbf{OG} = \frac{(\mathbf{OD} \times \mathbf{s}_{13}) \times (\mathbf{OE} \times \mathbf{s}_{23})}{s_{22} \cdot (\mathbf{OD} \times \mathbf{s}_{13})} \quad (41)$$

where  $\mathbf{OD}$  represents the coordinates of the center point  $U_1$  in the global coordinate system, and  $\mathbf{OE}$  represents the coordinates of the center point  $U_2$  in the global coordinate system. The distance from point  $G$  to the constraint force provided by the third branch, denoted as  $d_{GM}$ , can be obtained by the following formula:

$$d_{GM} = |\mathbf{OF} \times \mathbf{s}_{33} + (-\mathbf{OG}) \times \mathbf{s}_{33}| \quad (42)$$

where  $\mathbf{OF}$  represents the coordinates of the center point  $U_3$  in the global coordinate system. When  $d_{GM} = 0$ , it indicates that the three constraint forces intersect at a single point in a coplanar condition, resulting in a constraint singularity.

The relationship between the mechanism parameters and the angular displacement of the moving platform at the time of platform singularity is shown in Figure 13.

In conclusion, when designing rehabilitation mechanisms, in order to prevent the occurrence of limb kinematics singularities and platform constraint singularities, it is necessary to ensure that the angle of rotation of the moving platform  $\beta$  and the angle  $\delta_1$  between the rotational axes  $r_{i2}$  and  $r_{i5}$ , satisfy the relationship as shown in equation (43).

$$\theta + \frac{\beta}{2} < 90^\circ \quad (43)$$

### 3.2.5. Workspace

We solve the workspace with the prismatic pair travel as a constraint and use a cylindrical coordinate system to describe its workspace, where  $h_g$  at each layer is composed of a polar coordinate system. The parameters  $\alpha$  represents the polar angle, and parameter  $\beta$  represents the polar diameter, and select  $\beta = 0$  as the pole of the polar coordinate system. The final workspace of the mechanism was obtained, as shown in Figure 14. It was found that the range of kinematics meets the requirements and that there is no singularity within the internal workspace.

## 4. Motion/force transmission performance index

Performance index for force transmission encompasses input transmission performance index (ITI), output transmission performance index (OTI), input constraint performance index (ICI), and output constraint performance index (OCI). These indices can be used to evaluate the kinematics performance

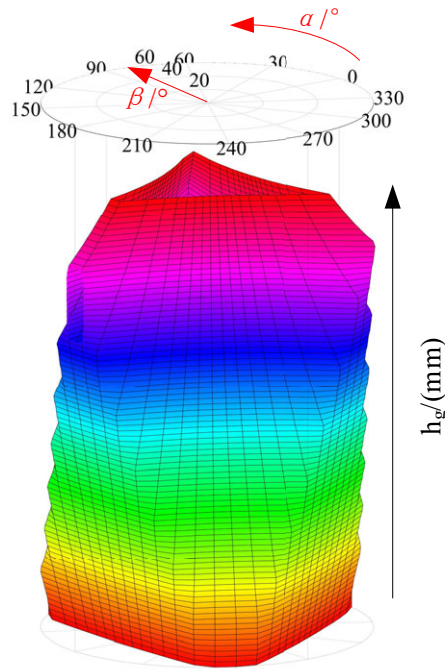


Figure 14. Workspace.

and stiffness of mechanisms, allowing for the optimization of the mechanism parameters based on the force transmission performance index. Next, we will analyze these four indices in detail.

#### 4.1. Input transmission performance index

The input transmission performance of the mechanism can be characterized by the power of the actuation force exerted by the limb along the direction of the actuation joint. Each PUU limb is equipped with five kinematics screws, denoted as  $\$_{ij} (1 \leq i \leq 3, 1 \leq j \leq 5)$ , as shown in Figure 5. The unit kinematics screws of the five kinematics pairs in the  $i$ -th limb collectively form the kinematics screw system  $\{H_i\}$  of that limb.

$$\{H_i\} = \{ \$_{i1} \quad \$_{i2} \quad \$_{i3} \quad \$_{i4} \quad \$_{i5} \}^T \quad (44)$$

When all the screws in the limb  $\{H_i\}$  are linearly independent, there exists a unique screw that is reciprocal to all the screws in the limb screw system, which yields:

$$\$_{ci} \circ \$_{ij} = 0 \quad (45)$$

$\$_{ci}$  is the constraint screw provided by one of the limbs of the PUU mechanism, passing through a point  $D_i$  on the intermediate constraint plane and parallel to  $\$_{i2}$ , known as the constraint wrench screw. When we select  $P$  pair of the limb as the driver and lock it, the rank of the kinematics screw system decreases. By solving for the inverse screws of the remaining four kinematics screws, we can determine the actuation screw of limb  $i$ .

$$\$_{Hi} \circ \$_{ij} = \begin{cases} 0, & j \neq 3 \\ 1, & j = 3 \end{cases}, i = 1, 2, 3, j = 1, 2, \dots, 5 \quad (46)$$

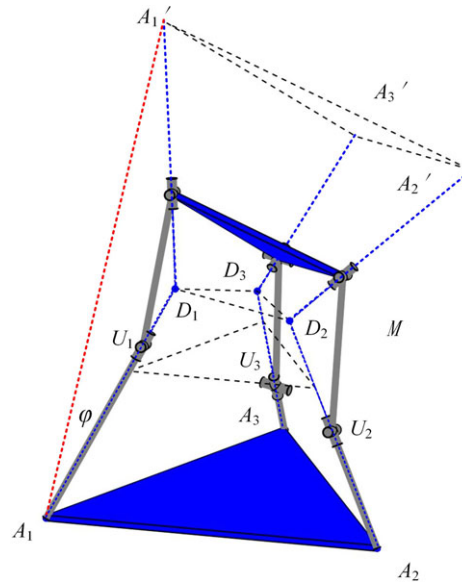


**Figure 15.** Geometric parameters of the 3-PUU parallel mechanism.

It can be obtained:

$$\$_{H,i} = (0 \quad e \quad b-a; \quad ac \quad 0 \quad 0)^T \quad (47)$$

We define the input transmission performance of limb  $i$  as the power generated by actuation wrench screw  $\$_{H,i}$  on the actuation joint screw  $\$_{I,i}$ . The index of ITI represents the ratio of instantaneous power to maximum power, that is:

$$\varepsilon_i = \frac{|\$_{H,i} \circ \$_{I,i}|}{|\$_{H,i} \circ \$_{I,i}|_{\max}} \quad (48)$$

The minimum value of input transmission performance for the three limbs is calculated based on equation (49), where  $\varepsilon = \min\{\varepsilon_1, \varepsilon_2, \varepsilon_3\}$  is selected as the optimal index for input transmission performance.

#### 4.2. Output transmission index

The output transmission performance can be described as the power of the actuating screws of the limbs to moving platform. Therefore, the force screw system acting on the moving platform of the 3-PUU parallel mechanism

$$\{\$_m\} = [\$_{c,1} \quad \$_{c,2} \quad \$_{c,3} \quad \$_{H,1} \quad \$_{H,2} \quad \$_{H,3}] \quad (49)$$

Since the coordinates of point  $\{\$_m\}$  are defined with respect to a fixed coordinate system  $\{O\}$ , it becomes necessary for points  $\$_{c,i}$  and  $\$_{H,i}$  to also be described within a fixed coordinate system. Consequently, it is required to solve for the coordinates of points  $D_i$  and  $U_i$ . The coordinates of point  $U_i$  can be obtained through the inverse kinematics of the 3-PUU parallel mechanism. The determination of the coordinates of  $D_i$  poses challenges in the analytical solution using the kinematics screw theory. Therefore, in this study, the coordinates of  $D_i$  are calculated using a geometric method.

Through the geometric relationship of the 3-PUU parallel mechanism, we take plane  $\triangle A_1'A_2'A_3'$  as the symmetric plane of plane  $M$  with respect to point  $\triangle A_1A_2A_3$ , as shown in Figure 15. Assuming that points  $A_1'$ ,  $A_2'$ , and  $A_3'$  are fixed on the moving platform, by coordinate transformation on the coordinates of the center point  $P$  of the moving platform, the coordinates of these three points in the fixed coordinate

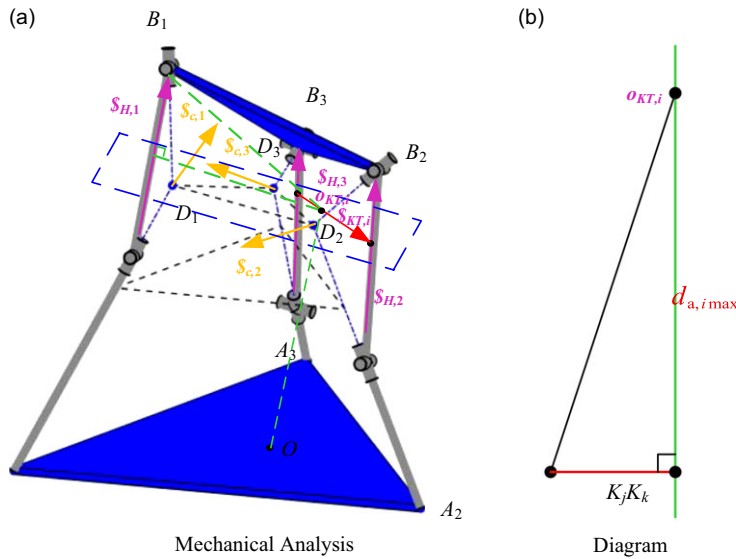


**Figure 16.** Mechanical analysis of a 3-PUU parallel mechanism.

system  $\{O\}$  can be acquired. According to the geometric constraints, the angle between vectors  $A_i A_i'$  and  $I_{AC,i}$  is:

$$\varphi_i = \arctan 2 \left( |A_i A_i' \times I_{AU,i}|, A_i A_i' \cdot I_{AU,i} \right) \quad (50)$$

Based on Equation (39) and the unique geometric features of the 3-PUU parallel mechanism, the coordinates of point  $D_i$  in the fixed coordinate system  $\{O\}$  can be determined as

$${}^O D_i = {}^O A_i + |A_i D_i| I_{AU,i} = {}^O D_i + \frac{|A_i A_i'|}{2 \cos \varphi_i} I_{AU,i} \quad (51)$$

In order to obtain the kinematics screw  $\$_{KT,i}$  of the moving platform that corresponds to the  $i$ -th limb actuation screw  $\$_{H,j}$ , one can lock the  $i$ -th limb actuation screw and solve for the inverse screws of the remaining five limbs individually.

$$\$_{KT,i} = \{ \$_{c,1} \quad \$_{c,2} \quad \$_{c,3} \quad \$_{H,j} \quad \$_{H,k} \}^r \quad (52)$$

In the equation, let  $i, j, k = 1, 2, 3$  and  $i \neq j \neq k$ . According to the definition of the inverse screw, it is evident that the lead screw  $\$_{KT,i}$  is in the same plane as each wrench screw within the assembly  $\{ \$_{c,1} \quad \$_{c,2} \quad \$_{c,3} \quad \$_{H,j} \quad \$_{H,k} \}$ . Assuming that  $\$_{H,j}$  intersects with the middle constraint plane  $M$  at point  $K_j$ , as shown in Figure 16a, then if  $\$_{H,k}$  intersects with the middle constraint plane  $M$  at point  $K_k$ , it follows that the kinematic screw  $\$_{KT,i}$  represents the motion rotating around the axis where the vector  $K_j K_k$  is located.

For the  $i$ -th limb of the 3-PUU parallel mechanism, the criterion for assessing output transmission performance is the power delivered from the actuation wrench screw  $\$_{H,i}$  to the kinematics screw  $\$_{KT,i}$  on the moving platform. The OTI demonstrates the proportional relationship between instantaneous power and maximum power, which is to say:

$$\eta_i = \frac{|\$_{H,i} \circ \$_{KT,i}|}{|\$_{H,i} \circ \$_{KT,i}|_{\max}} = \frac{d_{H,i} \sin \sigma_i}{d_{H,i \max}} = \frac{G_i H_i}{B_i G_i} \quad (53)$$

where, angle  $\sigma_i$  represents the angle between  $G_iH_i$  and  $B_iG_i$ . In Equation (45), it is only necessary to solve for the distance from point  $B_i$  to screw  $\$_{KT,i}$ , and  $\$_{KT,i}$  can be expressed as:

$$\$_{KT,i} = (\$_{KT,i}^T; \$_{OKT,i}^T)^T \quad (54)$$

The coordinates of point  $o_{ST,i}$ , the foot of the perpendicular from the origin  $O$  of the fixed coordinate system to the screw  $\$_{KT,i}$

$$o_{ST,i} = \frac{\$_{KT,i}^T \times \$_{OKT,i}^T}{\$_{KT,i}^T \cdot \$_{KT,i}^T} \quad (55)$$

The solution for  $d_{a,i \max}$  can be simplified as shown in Figure 16b.

Therefore:

$$d_{a,i \max} = |\$_{KT,i} \times o_{ST,i} B_i| \quad (56)$$

Let  $\eta = \min\{\eta_1, \eta_2, \eta_3\}$  be taken as the output performance index for optimality.

### 4.3. Input constraint performance index

The performance constraint of the mechanism input can be described as the power output of the limb constraint during the constrained kinematics process. Each PUU limb has five actuation screws. By calculating the inverse screws through these five actuation screws, we can determine the constraint screws of each limb. If these five actuation screws are sequentially set as driven and a driven one is fixed, an additional actuation screw is generated every time a lead screw is calculated in the screw system. As a result, a total of five additional actuation screws are obtained. These actuation screws do not produce power output on the limb constraint kinematics, and their calculation can be performed using Equation (46).

$$\$_{R,ij} = \left\{ \prod_{k \neq j}^{k=1, \dots, 5} \$_{ik} \right\}^T - \{ \$_{c,i} \} \quad (57)$$

In the equation,  $\prod_{k \neq j}^{k=1, \dots, 5} \$_{ik}$  represents the set of  $\$_{ik}$  when  $k = 1, \dots, 5$  and  $k \neq j$ .

By further solving the inverse screws  $\$_{RR,i}$  for these five screws, we obtain the reciprocal screws that are constrained by the constraint force screw  $\$_{c,i}$ .

$$\$_{RR,i} = \{ \$_{R,i1} \quad \$_{R,i2} \quad \$_{R,i3} \quad \$_{R,i4} \quad \$_{R,i5} \}^T \quad (58)$$

For limb  $i$  of the 3-PUU parallel mechanism, its input constraint performance can be defined as the power output of the constraint wrench screw  $\$_{c,i}$  while acting upon the actuation screw  $\$_{RR,i}$  in its corresponding screw kinematics. The ICI is then used to measure the ratio between instantaneous power and maximum power. That is:

$$\mu_i = \frac{|\$_{c,i} \circ \$_{RR,i}|}{|\$_{c,i} \circ \$_{RR,i}|_{\max}} = |\cos \psi| \quad (59)$$

Let  $\mu = \min\{\mu_1, \mu_2, \mu_3\}$  be designated as the optimal indices of the input constraint performance. It is found that due to the axes of  $\$_{c,i}$  and  $\$_{RR,i}$  being consistently aligned, their angle  $\psi_i$  is zero. This ensures that the constraint wrench screw of the 3-PUU parallel mechanism consistently aligns with the direction of the constraints, causing the power output of the limb constraint screw on the actuation screw to always be at its maximum. Consequently,  $\mu$  is perpetually equal to 1.

### 4.4. Output constraint performance index

The output constraint performance of the mechanism can be described as the power generated by the limb constraint during the restricted kinematics of the moving platform. This reciprocal screw represents

the constraint kinematics screw  $\$_{KC,i}$  of the moving platform under the constraint of the constraint screw.

$$\$_{KC,i} = \{ \$_{c,j} \quad \$_{c,k} \quad \$_{a,1} \quad \$_{a,2} \quad \$_{a,3} \}^T \quad (60)$$

where,  $i, j, k = 1, 2, 3$  and  $i \neq j \neq k$ .

At this moment,  $\$_{KC,i}$  is a general kinematics screw that can be expressed as:

$$\$_{KC,i} = (S_{KC,i}^T; S_{0KC,i}^T)^T \quad (61)$$

The maximum work power exerted by the constraint wrench screw on the moving platform is:

$$|\$_{c,i} \circ \$_{KC,i}|_{\max} = \sqrt{h_{KC,i}^2 + d_{c,i \max}^2} \quad (62)$$

where  $h_{KC,i}$  can be determined using the same method as that for solving Equation (52), with the approach being identical to that used for  $d_{a,i \max}$ .

$$h_{KC,i} = \frac{S_{KC,i}^T \cdot S_{0KC,i}}{S_{KC,i}^T \cdot S_{KC,i}} \quad (63)$$

The output constraint performance of the  $i$ -th limb can be understood as the power generated by the constraint screw  $\$_{c,i}$  in suppressing the kinematics screw  $\$_{KC,i}$  of the moving platform. The OCI then describes the ratio between the instantaneous power and the maximum power, that is:

$$\varsigma_i = \frac{|\$_{c,i} \circ \$_{KC,i}|}{|\$_{c,i} \circ \$_{KC,i}|_{\max}} \quad (64)$$

Select  $\varsigma = \min\{\varsigma_1, \varsigma_2, \varsigma_3\}$  as the optimal performance index for Output Constraint

#### 4.5. Optimal parameter valuation

From the definition of performance index, it is evident that a smaller indices value signifies less power generated by the actuation force in the direction of kinematics or a smaller amount of power done by the constraint force in the restricted direction of movement. This suggests poorer kinematics performance of the mechanism, potentially even approaching singular configuration. The local transmission index (LTI) is employed to describe the minimum value of the transmission performance index when  $h_g$  is fixed and the two kinematics parameters,  $\alpha$  and  $\beta$ , are varied. The local constraint index (LCI) describes the minimum value of input and output constraint performance under the same conditions. For the 3-PUU parallel mechanism, we can ascertain its suboptimal performance posture within the kinematics space by analyzing the behavior of LTI and LCI across the space. This approach allows us to identify postures within the 3-PUU kinematics space where its performance is lacking and to optimize the kinematics parameter  $h_g$  when the mechanism is at its poorest performing posture, ensuring stable operation across various working conditions.

Based on the analysis of the performance indices ITI, OTI, ICI, and OCI for the 3-PUU parallel mechanism in Section 3.3, we can obtain the LTI  $\kappa$  and the LCI  $\chi$  for the 3-PUU parallel mechanism as follows:

$$\begin{aligned} \kappa &= \min\{\varepsilon, \eta\} \\ \chi &= \min\{\mu, \varsigma\} \end{aligned} \quad (65)$$

The values of  $\kappa$  and  $\chi$  indices have a greater capability for force/motion transmission and a superior performance in terms of force/motion constraints. The fundamental structural parameters of the 3-PUU parallel mechanism size parameters are shown in Table 2, while the range of kinematics parameters for the 3-PUU parallel mechanism has been set to  $\alpha \in [0^\circ, 360^\circ]$ ,  $\beta \in [0^\circ, 46^\circ]$ , and  $h_g = 60$  mm. Figure 17 reveals the analysis results of the local transmission performance index and the local constraint performance index for the 3-PUU parallel mechanism within the specified range of motion.



Table II. Parameters of the 3-PUU parallel mechanism.

Parameters	$R/(\text{mm})$	$r/(\text{mm})$	$e/(\text{mm})$	$\gamma/\text{rad}$
Value	195	110	155	$\pi/3$

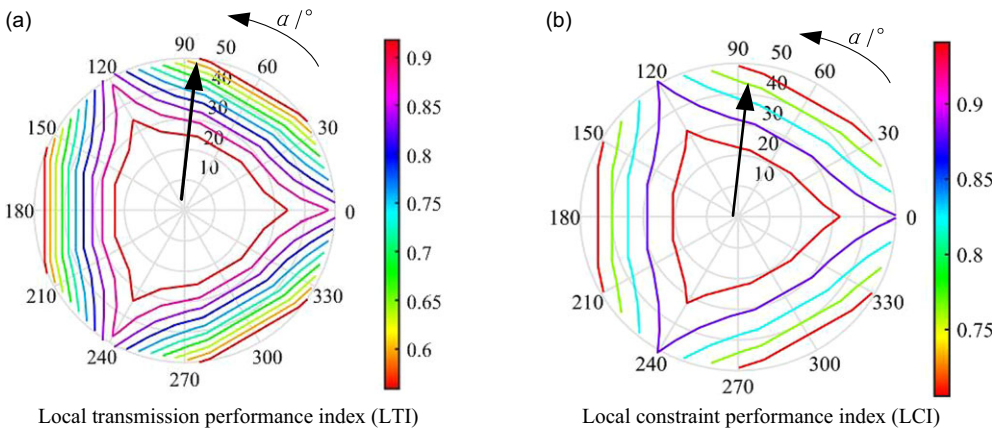


Figure 17. Local performance index.

Due to the symmetrical arrangement of the limbs within the mechanism, and their uniform distribution along the circular path on both the moving and fixed platforms, the LTI contour map also exhibits a  $120^\circ$  rotationally symmetric distribution around the circular path. According to the legend colors, as the color of the contour lines approaches red, the  $\kappa$  and  $\chi$  values of the mechanism decrease, while as the color moves towards pink, the  $\kappa$  and  $\chi$  values increase. By analyzing the LTI and LCI performance contour maps of the 3-PUU parallel mechanism, we discovered that when  $\alpha \in \{60^\circ, 180^\circ, 300^\circ\}$  and  $\beta > 46^\circ$ , the kinematics performance of the mechanism deteriorates, however, it still manages to stay away from singular positions. This indicates that the better the force/motion transmission performance and force/motion constraint performance, the more capable the mechanism is of performing full-circle movement.

5. Ankle joint rehabilitation robot parameter optimization

5.1. Determination of the size parameter range

The 3-PUU/R hybrid parallel mechanism is selected as the ankle rehabilitation device, and the selection of its dimensional parameters needs to meet the wearing requirements of the human body while ensuring the range of ankle joint motion. The relevant dimensions of the lower limb of the human body are presented in Table 3. Based on the analysis of the overall structure, to achieve a compact design with a simple structure, the following three parameters need to be optimized: (1) the distance  $R$  from the connection point of the fixed platform prismatic pair to the platform center; (2) the distance  $r$  from the center point of the lower U joint on the moving platform to the platform center; (3) the length  $|U_iB_i|$  of the link; and (4) the angle  $\theta$  between the prismatic pair and the platform:

Firstly, the constraint relationship between the moving platform size and the patient foot width was analyzed. Considering that the patient’s foot is fixed at the center position of the moving platform, the structural dimensions of the U pair itself must also be taken into account, as shown in Figure 18a.

According to the width of the human foot, the relationship that the size of the moving platform should meet is shown in Equation (66).

$$2 \times r \times \sin 60^\circ - h - hu \geq H \tag{66}$$

**Table III.** Human lower limb part relevant parameters.

Structural Name	Size Range
Calf length $h_t$	324–420mm
Ankle height $h_g$	60–75mm
Foot width $H$	86–106mm
Foot length $L$	223–271mm

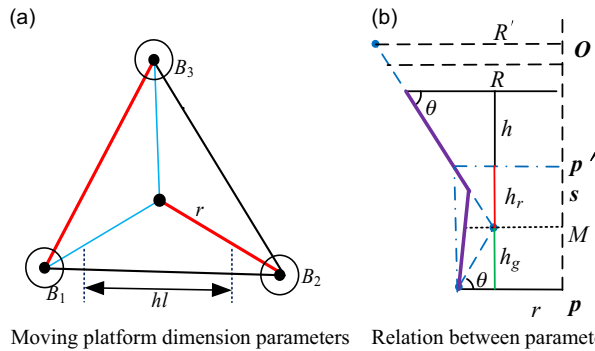


**Figure 18.** Relationship among the mechanism parameters.

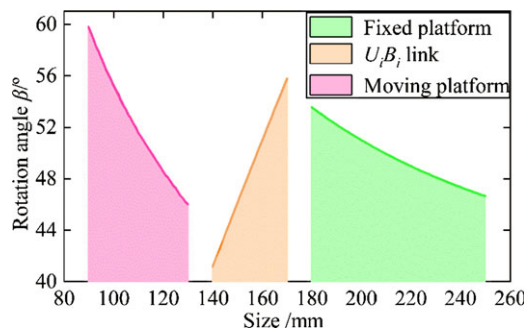


**Figure 19.** Relationship between the angle  $\beta$  and the  $R$  of the fixed platform.

$$2r \cos 30^\circ - h - \frac{\sqrt{h_t^2 + h_w^2}}{2} \geq H \quad (67)$$

where  $H$  represents the footprint width of a human body;  $h$  for the distance between  $U$  and the footprint;  $h_u$  for the width of the  $U$  component.

By substituting the relevant parameters into Equation (67), the mechanism parameter  $r \geq 90\text{mm}$  can be obtained. Under the condition that the size and angle of the fixed platform remain unchanged, the relationship between the angle of the moving platform of the mechanism and its size can be analyzed based on the kinematics of the mechanism, as shown in Figure 19. Under the premise that the angle is greater than  $46^\circ$ , the size of the moving platform should meet  $90\text{mm} \leq r \leq 130\text{mm}$ .

The parameter  $\theta$  are determined based on the constraint condition of platform singularity during the analysis of mechanism singularity. When the constraints of the three limbs coincide at one point, an occurrence of increased DOFs and control instability. The relationship between mechanism parameter  $\theta$  and the angle  $\beta$ , obtained from the mechanism singularity analysis, is presented in Equation (68):

$$2\theta + \beta < 180^\circ \quad (68)$$

Finally, the parameter  $\theta$  is determined to be  $55^\circ \leq \theta \leq 65^\circ$  according to the constraint conditions.

Under the condition that the angle  $\theta$  and the size of the moving platform  $r$  remain unchanged, the increase of the fixed platform parameter will lead to the increase of the mechanism parameter  $h_g$ . The relationship between parameters  $R$  and mechanism parameters  $r, \theta$  is shown in Figure 19.

$$(R - r) \times \tan \theta + h_r + h_g \leq h_t \quad (69)$$

By substituting the relevant parameters into Equation (69), the mechanism parameter  $R \geq 180\text{mm}$  can be determined. Subsequently, the relationship between the obtained mechanism angle  $\beta$  and the fixed platform  $R$ , as shown in Figure 18, was obtained through kinematics analysis.

Through the aforementioned two constraint relationships, the final constraint condition for determining parameter  $R$  is set as  $180\text{mm} \leq R \leq 230\text{mm}$ .

As shown in Figure 18, the length of the link  $h_g$  between the two U pairs satisfies the following relationship:  $h_g < |U_i B_i|$ . Additionally, the relationship between the angle  $\beta$  of the mechanism and the length  $|U_i B_i|$  of the link is shown in Figure 18, which is derived from kinematics inverse. This leads to the final determination of constraint condition  $148\text{mm} \leq |U_i B_i| \leq 165\text{mm}$ .

Finally, the overall optimal range size parameters of the ankle joint rehabilitation mechanism were obtained, as shown in Equation (70).

$$\begin{cases} 180\text{mm} \leq R \leq 230\text{mm} \\ 55^\circ \leq \theta \leq 65^\circ \\ 90\text{mm} \leq r \leq 130\text{mm} \\ 148\text{mm} \leq |U_i B_i| \leq 165\text{mm} \end{cases} \quad (70)$$

## 5.2. Optimization of ankle joint rehabilitation mechanism

### 5.2.1. Design index

Considering the transmission performance and constraint performance of the mechanism, the optimal design is carried out. The local design index (LDI) is defined:

$$\text{LDI} = \min \{ \text{LTI}, \text{TCI} \} \quad (71)$$

The higher the value of LDI in a mechanism, the better its transmission and constraint performance at that pose. To evaluate the global transmission and constraint performance of the mechanism, the good performance workspace (GPW) is defined where  $\text{LDI} \geq 0.7$ . Within GPW, the mechanism has good performance and is far from singularity [33]. Subsequently, we define the global design index (GDI) of the mechanism over the entire GPW as:

$$\text{GDI} = \frac{\int \text{LDI} \cdot dW_a}{\int \text{LDI} \cdot dW_b} \quad (72)$$

where  $dW_a$  denotes the GPW with  $\text{LDI} \geq 0.9$ ,  $dW_b$  denotes the GPW with  $\text{LDI} \geq 0.7$ .

The higher the GDI value, the better the overall transmission/constraint performance of the mechanism within the GPW.

### 5.2.2. Dimensional synthesis

Optimize the 3-PUU mechanism with three parameters:  $r, R, |U_i B_i|$ . There is no analytical expression between these design parameters and the overall performance index. Liu [34] proposed a method based on performance mapping which can intuitively display the relationship between them, thus enabling the optimization of the mechanism design.

First of all, the three parameters are processed without dimension, and the results are obtained:

$$D = \frac{(r + R + |U_i B_i|)}{3} \quad (73)$$

Table IV. Results of overloading for 3 Experimental setups.

	$p$	$q$	$r_1$	$r_2$	$r_3$
A	0	$\frac{3}{2}\sqrt{2}$	0	3	0
B	0	0	0	$\frac{3}{2}$	$\frac{3}{2}$
C	$\frac{15}{34}\sqrt{6}$	0	$\frac{15}{17}$	$\frac{18}{17}$	$\frac{18}{17}$

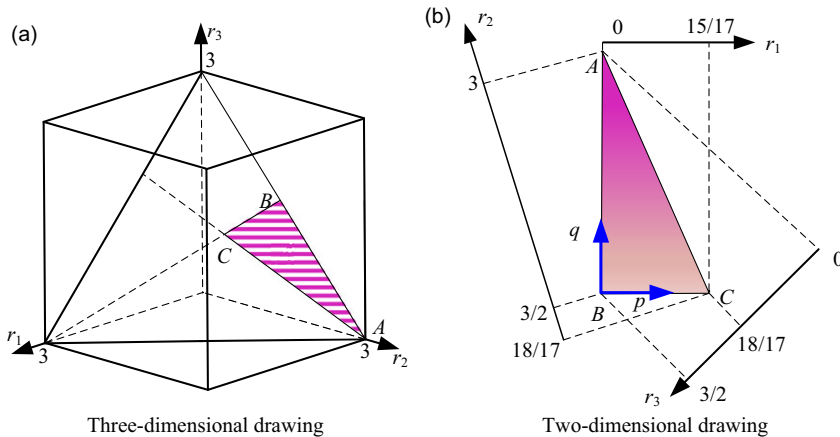


Figure 20. Parameter design space.

$$r_1 = \frac{r}{D}, r_2 = \frac{R}{D}, r_3 = \frac{|U_i B_i|}{D} \quad (74)$$

Based on the human wearing requirements and the optimal range size parameters of the ankle joint rehabilitation mechanism, the following are obtained.

$$\begin{cases} 0 < r_1, r_2, r_3 < 3 \\ r_1 + r_2 + r_3 = 3 \\ r_3 < r_2 \\ 1.2r_1 < r_3 \end{cases} \quad (75)$$

Through Equation (75), by taking  $r_1$ ,  $r_2$ , and  $r_3$  as coordinate axes, a planar area  $ABC$  can be determined, which represents the parameter design space for the ankle joint rehabilitation mechanism, as shown in Figure 20a. Within this parameter design space, each point corresponds to a set of dimensions for the mechanism. Using this parameter design space, one can establish the relationship between the optimization index and the geometric parameters of the mechanism.

The two-dimensional form of parameter design space of rehabilitation mechanism is shown in Figure 20b. The data relationship between  $(r_1, r_2, r_3)$  and  $(p, q)$  is as follows:

From the relationships in Table 4, we can express the connection between  $(r_1, r_2, r_3)$  and  $(p, q)$  as follows:

$$\begin{cases} r_1 = \frac{\sqrt{6}}{3}p \\ r_2 = -\frac{\sqrt{6}}{6}p + \frac{\sqrt{2}}{2}q + \frac{3}{2} \\ r_3 = -\frac{\sqrt{6}}{6}p - \frac{\sqrt{2}}{2}q + \frac{3}{2} \end{cases} \quad (76)$$

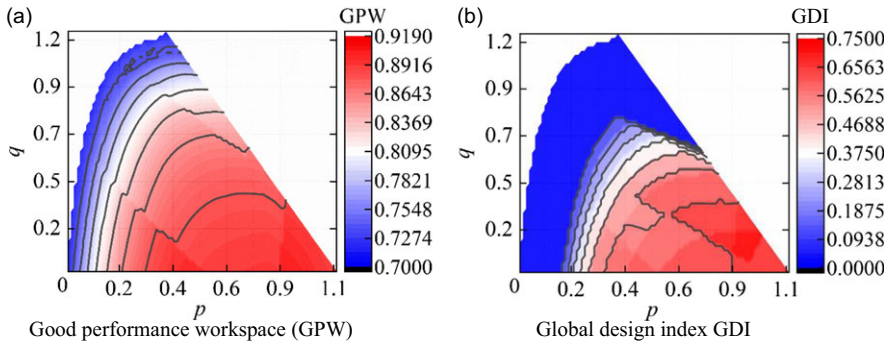


**Figure 21.** Mechanism performance.

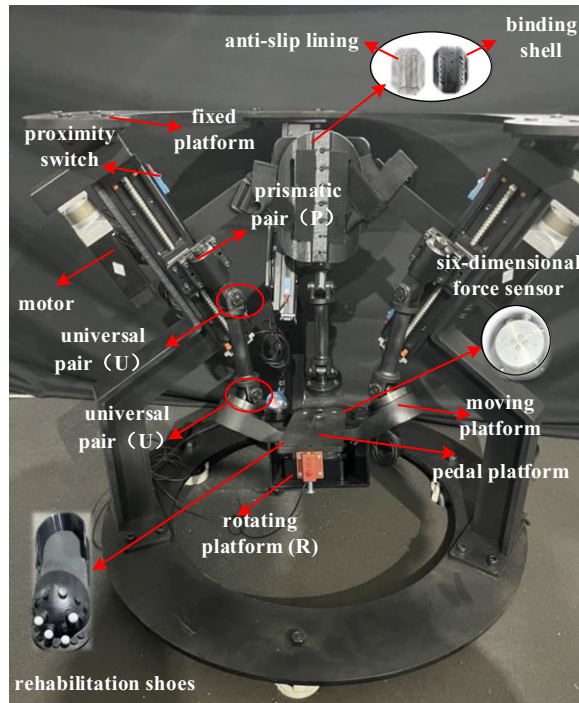


**Figure 22.** Ankle joint rehabilitation prototype.

According to the definitions of GPW and GDI, the optimal design diagram of rehabilitation mechanism in the parameter design space is shown in Figure 21.

It can be seen in Figure 21a and Figure 21b that the indices of GPW and GDI are better when the indices are closer to the right end of  $p$  value and the  $q$  value is closer to the lower end. The optimal region parameters for the design parameters are when  $p > 0.9$  and  $q < 0.2$ . Choosing  $p = 0.9513$  and  $q = 0.1484$ , according to equation (76), we get:  $r_1 = 0.7767$ ,  $r_2 = 1.2166$ ,  $r_3 = 1.0067$ . Combining Equation (74), setting  $D = 450$  mm, gives us  $r = 120$  mm,  $R = 195$  mm,  $|U_i B_i| = 155$  mm. The optimal design size of a group of rehabilitation mechanisms is obtained.

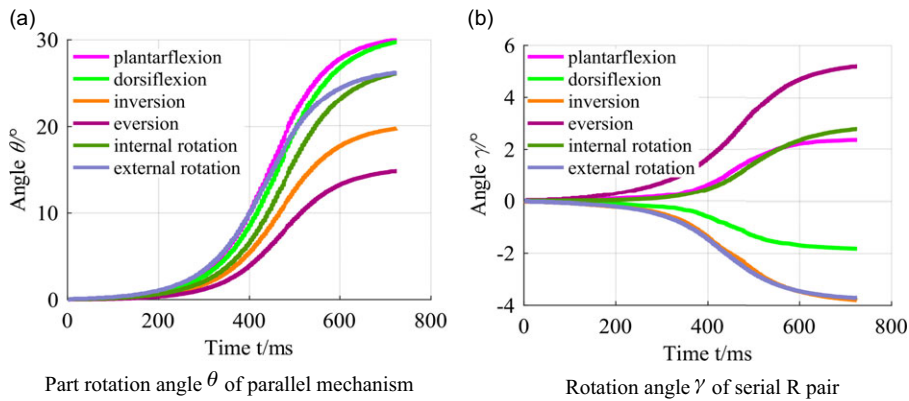


**Figure 23.** Range of motion of the ankle rehabilitation mechanism.

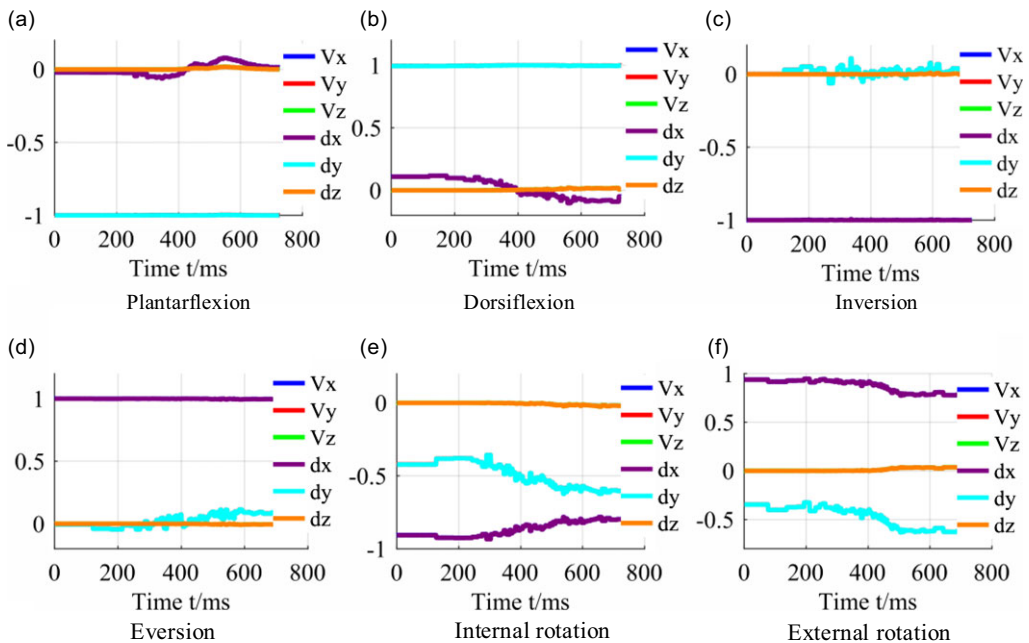


**Figure 24.** Unit speed and direction.

## 6. Prototype and experiment of ankle joint rehabilitation robot

This paper utilizes the Inovance model AM401-CPU1608TN programmable controller, which fully supports the IEC61131-3 programming system and supports EtherCAT real-time bus and synchronized motion control. It is equipped with high-speed IO ports, making it well-suited for high-speed applications. In the parallel section, the Inovance model MS1H4-10830CB-A334R 100W servo motor is used, achieving linear motor motion through the servo driver and synchronous belt reduction. In the  $R$  joint, the Inovance model MS1H4-05B30CB-A334R 50W servo motor is used, with the servo motor driving the turntable to complete the rotation of the  $R$  joint, all utilizing the Inovance model SV660NS1R61 driver. A six-dimensional force sensor produced by Ten-Kun Sensors is used for force and torque acquisition. The sensor features high rigidity, high resolution, low coupling, high precision, and a high protection level, with a maximum force load of 400 N, a maximum torque of 35 Nm, and an accuracy of 0.1–0.5% F.S. The ankle joint rehabilitation robot is displayed, as shown in Figure 22.



The same subjects as in chapter 2 were selected for the ankle rehabilitation training experiment, and the human ankle axis obtained in chapter 2 was used to make the mechanism move according to the ankle axis to verify the rehabilitation training effect of the mechanism. The ankle joint was trained with different rehabilitation exercise models, and the relationship between angle change and time was obtained, as shown in Figure 23. The variation curve of velocity and axis direction over time is obtained, as shown in Figure 24.

Based on Figure 23, it can be seen that the mechanism can meet the angular range requirements of different rehabilitation exercise modes. From Figure 24, it can be observed that the speed curve of the mechanism is generally consistent with the direction curve of the axis, indicating that the mechanism can move in accordance with the human ankle axis.

## 7. Conclusions

Based on the characteristics of ankle motion axis, this paper proposes a novel ankle joint rehabilitation mechanism from the perspective of human-machine axis fusion. Within a certain range, the mechanism can be continuously rotated around any axis in the spatial plane, that is, it can be rotated around the instantaneous axis of the ankle joint at a non-fixed point, thereby improving the rehabilitation effect, making it safer, and preventing secondary injuries. First, we used the motion capture system to identify and calculate the axis of human ankle joint motion. A 3-PUU/R serial-parallel ankle rehabilitation mechanism was designed based on the motion mode and range of human motion axis, and the kinematics analysis of the mechanism was carried out, including the mechanism kinematics inverse, complete Jacobian matrix, singularity, and workspace. Secondly, based on the motion/force transmission index and constraint index, the motion performance of the rehabilitation mechanism is analyzed, and it is proved that the rehabilitation mechanism has good transmission performance and constraint performance. Thirdly, the size range of the ankle joint rehabilitation robot is determined based on the needs of human wearing, and then the dimensional synthesis of the mechanism is carried out with  $r$ ,  $R$  and  $|U_i B_i|$  as the optimization parameters. Finally, the prototype of ankle joint rehabilitation is manufactured. The ability of the mechanism to achieve motion matching the axis of the human ankle joint was verified through experiments.

The proposed mechanism holds promising potential for enhancing the comfort and safety of ankle rehabilitation, ultimately leading to improved patient outcomes. Further research and development in this field will contribute to the advancement of ankle rehabilitation techniques.

**Supplementary material.** The supplementary material for this article can be found at <https://doi.org/10.1017/S0263574724001462>.

**Author contributions.** Xuechan Chen and Ziming Chen conceived and designed the study. Yu Guo and Bo Xiao conducted data gathering. Jianxin Liu and Jinan Dong performed experiments. Zhouhao Zhang designed the prototype. Xuechan Chen wrote the article.

**Financial support.** The research is supported by National Natural Science Foundation of China (Grant No. 51775474).

**Competing interests.** The authors declare no competing financial interests.

**Ethical approval.** The study has been approved by the Ethics Committee of Qinhuangdao First Hospital.

## References

- [1] M. Bozkurt, N. Apaydin and S. GURSOY, *Sports Injuries: Prevention, Diagnosis, Treatment and Rehabilitation* (Springer, Berlin Heidelberg, Berlin, 2015).
- [2] J. W. Smith, "The forces operating at the human ankle joint during standing," *J Anat* **91**(4), 545–564 (1957).
- [3] Y.-L. Zhu, "Study on standardized comprehensive rehabilitation treatment for stroke patients with hemiplegia," *Chinese J Rehabil Med* **20**(001), 68–69 (2005).
- [4] M. S. Ballal, C. J. Pearce and J. D. Calder, "Management of sports injuries of the foot and ankle: An update," *Bone Joint J* **98-b**(7), 874–883 (2016).



- [5] W. Chen, “Observation on the clinical effect of nerve loosening combined with rehabilitation training on ankle joint motor dysfunction after stroke,” *Foot Health Care* **28**(1004-6569), 70–71 (2019).
- [6] L.-Y. Zhang, “Observation on rehabilitation effect of ankle joint dysfunction,” *Chinese J Phys Med Rehabil* **25**(3), 139–139 (2003).
- [7] C.-K. Lin, M. S. Ju, S. Chen and B. Pan, “A specialized robot for ankle rehabilitation and evaluation,” *J Med Biol Eng* **28**(2), 79–86 (2008).
- [8] J. A. Saglia, N. G. Tsagarakis, J. S. Dai and D. G. Caldwell, “Control Strategies for Ankle Rehabilitation using a High Performance Ankle Exerciser,” **In: Control Strategies for Ankle Rehabilitation using a High Performance Ankle Exerciser** (2010) pp. 2221–2227. doi: [10.1109/ROBOT.2010.5509883](https://doi.org/10.1109/ROBOT.2010.5509883).
- [9] A. Agrawal, V. Sangwan, S. K. Banala, S. K. Agrawal and S. A. Binder-Macleod, “Design of a novel two degree-of-freedom ankle-foot orthosis,” *J Mech Design* **129**(11), 1137–1143 (2007).
- [10] M. Vallés, J. Cazalilla, Á. Valera, V. Mata, Á. Page and M. Díaz-Rodríguez, “A 3-PRS parallel manipulator for ankle rehabilitation: Towards a low-cost robotic rehabilitation,” *Robotica* **35**(10), 1939–1957 (2017).
- [11] J. Li, Y. Zhou, M. Dong, X. Rong and R. Jiao, “Clinically oriented ankle rehabilitation robot with a novel R-2UPS/RR mechanism,” *Robotica* **41**(1), 277–291 (2023).
- [12] E.-D. Flores-Salazar, E. Lugo-González, M. Arias-Montiel and J. Gallardo-Alvarado, “A robust control scheme for a 2PUS+RR parallel robot for ankle rehabilitation,” *Robotica* **41**(11), 3296–3313 (2023).
- [13] T.-C. Chang and X.-D. Zhang, “Kinematics and reliable analysis of decoupled parallel mechanism for ankle rehabilitation,” *Microelectron Reliab* **99**, 203–212 (2019).
- [14] C.-Z. Wang, Y.-F. Fang, S. Guo and C. C. Zhou, “Design and kinematic analysis of redundantly actuated parallel mechanisms for ankle rehabilitation,” *Robotica* **33**(2), 366–384 (2015).
- [15] K. Shi, Z.-J. Wang, C.-T. Yan and Z.-W. Wang, “Design and performance analysis of the 4UPS-RRR parallel ankle rehabilitation mechanism,” *Mech Sci* **15**(2), 417–430 (2024).
- [16] Y. Liu, W. Lu, D. Fan, W. Tan, B. Hu and D. Zeng, “Type synthesis of self-alignment parallel ankle rehabilitation robot with suitable passive degrees of freedom,” *Chin J Mech Eng* **37**(1), 21 (2024).
- [17] T. Wang, E. Spyarakos-Papastavridis and J.-S. Dai, “Design and analysis of a novel reconfigurable ankle rehabilitation exoskeleton capable of matching the mobile biological joint center in real-time,” *J Mech Robot* **15**(1), 011011 (2022).
- [18] Y. Wang and M. Xiao, “Design and analysis of parallel ankle joint rehabilitation robot,” *Int J* **16**, 42–42 (2024).
- [19] J. Zhang, C. Liu, T. Liu, K. Qi, J. Niu and S. Guo, “Module combination based configuration synthesis and kinematic analysis of generalized spherical parallel mechanism for ankle rehabilitation,” *Mech Mach Theory* **166**, 104436 (2021).
- [20] M. Ni, J.-L. Liu, Z.-H. Sun and T. Sun, “Design and experiment of an ankle rehabilitation robot after fracture surgery,” *J Mech Robot* **16**(12), 121014–121026 (2024).
- [21] J. Dul and G. E. Johnson, “A kinematic model of the human ankle,” *J Biomed Eng* **7**(2), 137–143 (1985).
- [22] M. Bottlang, J. L. Marsh and T. D. Brown, “Articulated external fixation of the ankle: Minimizing motion resistance by accurate axis alignment,” *J Biomech* **32**(1), 63–70 (1999).
- [23] A. Lundberg, O. K. Svensson, G. Nemeth and G. Selvik, “The axis of rotation of the ankle joint,” *J Bone Joint Surg Br* **71-B**(1), 94–99 (1989).
- [24] A. Lundberg, I. Goldie, B. Kalin and G. Selvik, “Kinematics of the ankle/foot complex: Plantarflexion and dorsiflexion,” *Foot Ankle* **9**(4), 194–200 (1989).
- [25] O. Rasmussen and I. Tovborg-Jensen, “Mobility of the ankle joint: Recording of rotatory movements in the talocrural joint in vitro with and without the lateral collateral ligaments of the ankle,” *Acta Orthop Scand* **53**(1), 155–160 (1982).
- [26] E. J. V. Langelan, “A kinematical analysis of the tarsal joints. An X-ray photogrammetric study,” *Acta Orthop Scand* **204**, 1–269 (1983).
- [27] S. Siegler, J. Chen and C. D. Schneck, “The three-dimensional kinematics and flexibility characteristics of the human ankle and subtalar joints—part I: Kinematics,” *J Biomech Eng* **110**(4), 364–373 (1988).
- [28] A. Leardini, J.-J. O’Connor, F. Catani and S. Giannini, “Kinematics of the human ankle complex in passive flexion; a single degree of freedom system,” *J Biomech* **32**(2), 111–118 (1999).
- [29] L. Beimers, G. J. Maria Tuijthof, L. Blankevoort, R. Jonges, M. Maas and C. N. van Dijk, “In-vivo range of motion of the subtalar joint using computed tomography,” *J Biomech* **41**(7), 1390–1397 (2008).
- [30] F.-T. Sheehan, “The instantaneous helical axis of the subtalar and talocrural joints: A non-invasive in vivo dynamic study,” *J Foot Ankle Res* **3**(1), 13 (2010).
- [31] A.-I. Farkapandji, Functional anatomy of bone and joint, (2011).
- [32] Y. Fang and L.-W. Tsai, “Structure synthesis of a class of 4-dof and 5-dof parallel manipulators with identical limb structures,” *Int J Robot Res* **21**(9), 799–810 (2002).
- [33] J.-K. Song, C. Zhao, K. Zhao, W.-J. Yan and Z.-M. Chen, “Singularity analysis and dimensional synthesis of a 2R1T 3-UPU parallel mechanism based on performance atlas,” *J Mech Robot* **15**(1), 001–011 (2022).
- [34] X.-J. Liu and J. Wang, “A new methodology for optimal kinematic design of parallel mechanisms,” *Mech Mach Theory* **42**(9), 1210–1224 (2007).

**Cite this article:** X. Chen, J. Liu, J. a. Dong, Z. Zhang, Y. Guo, B. Xiao and Z. Chen (2024). “Analysis and optimization design of motion characteristics for a 3-PUU/R parallel ankle joint rehabilitation mechanism”, *Robotica* **42**, 3450–3479. <https://doi.org/10.1017/S0263574724001462>